





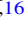











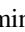
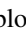




OPEN ACCESS

MINDS: The JWST MIRI Mid-INfrared Disk Survey

Thomas Henning^{1,27} , Inga Kamp^{2,27} , Matthias Samland¹ , Aditya M. Arabhavi² , Jayatee Kanwar^{2,3,4} ,
Ewine F. van Dishoeck^{5,6} , Manuel Güdel^{7,8} , Pierre-Olivier Lagage⁹, Christoffel Waelkens¹⁰, Alain Abergel¹¹,
Olivier Absil¹² , David Barrado¹³ , Anthony Boccaletti¹⁴, Jeroen Bouwman¹ , Alessio Caratti o Garatti^{15,16} ,
Vincent Geers¹⁷ , Adrian M. Glauser⁸ , Fred Lahuis¹⁸, Michael Mueller¹⁹ , Cyrine Nehmé⁹, Göran Olofsson²⁰ , Eric Pantin⁹,
Tom P. Ray¹⁶ , Silvia Scheithauer¹ , Bart Vandenbussche¹⁰ , L. B. F. M. Waters^{21,22} , Gillian Wright¹⁷,
Ioannis Argyriou¹⁰ , Valentin Christiaens^{10,12} , Riccardo Franceschi¹, Danny Gasman¹⁰ , Sierra L. Grant⁶ ,
Rodrigo Guadarrama⁷, Hyerin Jang²¹, Maria Morales-Calderón¹³ , Nicole Pawellek^{7,23} , Giulia Perotti¹ ,
Donna Rodgers-Lee¹⁶ , Jürgen Schreiber¹, Kamber Schwarz¹ , Benoît Tabone¹¹, Milou Temmink⁵ , Marissa Vlasblom⁵ ,

Luis Colina²⁴, Thomas R. Greve²⁵, and Göran Östlin²⁶

¹ Max-Planck-Institut für Astronomie (MPIA), Königstuhl 17, 69117 Heidelberg, Germany

² Kapteyn Astronomical Institute, University of Groningen, 9700 AV Groningen, The Netherlands

³ Space Research Institute, Austrian Academy of Sciences, Schmiedlstr. 6, A-8042, Graz, Austria

⁴ TU Graz, Fakultät für Mathematik, Physik und Geodäsie, Petersgasse 16 8010 Graz, Austria

⁵ Leiden Observatory, Leiden University, P.O. Box 9513, 2333 CC Leiden, The Netherlands

⁶ Max-Planck Institut für Extraterrestrische Physik (MPE), Giessenbachstr. 1, 85748, Garching, Germany

⁷ Department of Astrophysics, University of Vienna, Türkenschanzstr. 17, A-1180 Vienna, Austria

⁸ ETH Zürich, Institute for Particle Physics and Astrophysics, Wolfgang-Pauli-Str. 27, 8093 Zürich, Switzerland

⁹ Université Paris-Saclay, Université Paris Cité, CEA, CNRS, AIM, F-91191 Gif-sur-Yvette, France

¹⁰ Institute of Astronomy, KU Leuven, Celestijnenlaan 200D, 3001 Leuven, Belgium

¹¹ Université Paris-Saclay, CNRS, Institut d'Astrophysique Spatiale, 91405, Orsay, France

¹² STAR Institute, Université de Liège, Allée du Six Août 19c, 4000 Liège, Belgium

¹³ Centro de Astrobiología (CAB), CSIC-INTA, ESAC Campus, Camino Bajo del Castillo s/n, 28692 Villanueva de la Cañada, Madrid, Spain

¹⁴ LESIA, Observatoire de Paris, Université PSL, CNRS, Sorbonne Université, Université de Paris, 5 place Jules Janssen, 92195 Meudon, France

¹⁵ INAF—Osservatorio Astronomico di Capodimonte, Salita Moiariello 16, 80131 Napoli, Italy

¹⁶ Dublin Institute for Advanced Studies, 31 Fitzwilliam Place, D02 XF86 Dublin, Ireland

¹⁷ UK Astronomy Technology Centre, Royal Observatory Edinburgh, Blackford Hill, Edinburgh EH9 3HJ, UK

¹⁸ SRON Netherlands Institute for Space Research, P.O. Box 800, 9700 AV, Groningen, The Netherlands

¹⁹ Kapteyn Astronomical Institute, Rijksuniversiteit Groningen, Postbus 800, 9700AV Groningen, The Netherlands

²⁰ Department of Astronomy, Stockholm University, AlbaNova University Center, 10691 Stockholm, Sweden

²¹ Department of Astrophysics/IMAPP, Radboud University, P.O. Box 9010, 6500 GL Nijmegen, The Netherlands

²² SRON Netherlands Institute for Space Research, Niels Bohrweg 4, NL-2333 CA Leiden, The Netherlands

²³ Konkoly Observatory, Research Centre for Astronomy and Earth Sciences, Eötvös Loránd Research Network (ELKH), Konkoly-Thege Miklós út 15-17, H-1121 Budapest, Hungary

²⁴ Centro de Astrobiología (CAB, CSIC-INTA), Carretera de Ajalvir, E-28850 Torrejón de Ardoz, Madrid, Spain

²⁵ DTU Space, Technical University of Denmark, Building 328, Elektrovej, 2800 Kgs. Lyngby, Denmark

²⁶ Department of Astronomy, Oskar Klein Centre; Stockholm University; SE-106 91 Stockholm, Sweden

Received 2024 January 17; accepted 2024 March 15; published 2024 May 16

Abstract

The study of protoplanetary disks has become increasingly important with the Kepler satellite finding that exoplanets are ubiquitous around stars in our galaxy and the discovery of enormous diversity in planetary system architectures and planet properties. High-resolution near-IR and ALMA images show strong evidence for ongoing planet formation in young disks. The JWST MIRI mid-INfrared Disk Survey (MINDS) aims to (1) investigate the chemical inventory in the terrestrial planet-forming zone across stellar spectral type, (2) follow the gas evolution into the disk dispersal stage, and (3) study the structure of protoplanetary and debris disks in the thermal mid-IR. The MINDS survey will thus build a bridge between the chemical inventory of disks and the properties of exoplanets. The survey comprises 52 targets (Herbig Ae stars, T Tauri stars, very low-mass stars and young debris disks). We primarily obtain MIRI/MRS spectra with high signal-to-noise ratio (~ 100 – 500) covering the complete wavelength range from 4.9 to 27.9 μm . For a handful of selected targets we also obtain NIRSpect IFU high

²⁷ Shared first authorship.



resolution spectroscopy (2.87–5.27 μm). We will search for signposts of planet formation in thermal emission of micron-sized dust—information complementary to near-IR scattered light emission from small dust grains and emission from large dust in the submillimeter wavelength domain. We will also study the spatial structure of disks in three key systems that have shown signposts for planet formation, TW Hya and HD 169142 using the MIRI coronagraph at 15.5 μm and 10.65 μm respectively and PDS 70 using NIRCcam imaging in the 1.87 μm narrow and the 4.8 μm medium band filter. We provide here an overview of the MINDS survey and showcase the power of the new JWST mid-IR molecular spectroscopy with the TW Hya disk spectrum where we report the detection of the molecular ion CH_3^+ and the robust confirmation of HCO^+ earlier detected with Spitzer.

Unified Astronomy Thesaurus concepts: [Pre-main sequence stars \(1290\)](#); [Protoplanetary disks \(1300\)](#); [T Tauri stars \(1681\)](#); [Low mass stars \(2050\)](#); [Herbig Ae/Be stars \(723\)](#)

1. Introduction

Over the last years, Kepler and now TESS have shown that the efficiency of planet formation has to be high, i.e., that every circumstellar disk around a young star is essentially forming planets. Recent near-IR imaging at 10 m class telescopes has revealed protoplanet candidates embedded in the birth environment of their disks (e.g., Gratton et al. 2019; Hammond et al. 2023) and led to the confirmed detection of one system with two massive protoplanets inside a dust gap, PDS 70 (Keppler et al. 2018; Müller et al. 2018). ALMA confirms the presence of a circumplanetary disk around PDS 70 c (Benisty et al. 2021). More indirectly, gas kinematics can indicate the potential presence of massive protoplanets in disks (Pinte et al. 2018, 2023; Teague et al. 2018). In addition, VLT/SPHERE, Gemini/GPI, Subaru and ALMA high-resolution images of planet forming disks show intriguing substructure that is often attributed to ongoing planet formation (e.g., dust traps, rings, gaps and spirals—Tamura 2009; van der Marel et al. 2013; ALMA Partnership et al. 2015; Benisty et al. 2015; van Boekel et al. 2017; Andrews et al. 2018; Rich et al. 2022). In young primordial disks, dust grains, gas and protoplanets interact with each other, leading to dust migration, trapping and thus producing this wealth of substructure (Andrews 2020; Birnstiel 2023).

In later stages of planet formation, both dust and gas are likely of secondary origin and could carry information on the composition of the planetesimals that are still contributing to the formation of terrestrial planets (Wyatt 2008). Herschel and ALMA spectroscopy found traces of gas left in young debris disks (e.g., Riviere-Marichalar et al. 2012; Roberge et al. 2013; Dent et al. 2014; Moór et al. 2017); some of these systems are harboring cold dust in Kuiper belts next to warm dust in asteroid belts (Matthews et al. 2014).

The next challenge in planet formation studies is to provide a connection between the chemical composition of disks in the gas and solids and the composition of planets and their atmospheres. All of these recent findings underline the importance of characterizing the current chemical composition and structure of disks during the entire planet forming phase (well into the debris disk stage) and linking it to the planetary

systems that are forming inside them (e.g., Mollière et al. 2022). This is the goal of the Guaranteed Time Observations (GTO) JWST MIRI mid-INfrared Disk Survey (MINDS, PI: Th. Henning), especially for the molecular inventory in the inner terrestrial planet-forming regions of disks. It bridges between the GTO programs that study embedded disks (JOYS, PI: E. van Dishoeck) and exoplanets (EXO, PI: P.-O. Lagage).

1.1. Scientific Goals of MINDS

We will use JWST to (1) investigate the chemical inventory in the terrestrial planet-forming zone across stellar spectral type, (2) follow the gas evolution into the disk dispersal stage, and (3) study the structure of protoplanetary and debris disks in the thermal mid-IR. The MINDS survey will thus build a bridge between the chemical inventory of disks and the properties of exoplanets. In the subsequent paragraphs, we outline these in more detail.

1.1.1. The Chemical Inventory

The program aims at a comprehensive characterization of the dust and gas content of disks during the entire planet-forming phase and across stellar spectral types (A0-M8). After Spitzer and ground-based detections of H_2O , OH, HCN, C_2H_2 and CO_2 (e.g., Carr & Najita 2008; Salyk et al. 2008; Pascucci et al. 2009, 2013; Pontoppidan et al. 2010; Mandell et al. 2012), we will search for less abundant/more complex molecules such as CH_4 , C_6H_6 , NH_3 , HCO^+ or HNC and rare isotopologues (e.g., $^{13}\text{CO}_2$, H_2^{18}O , HDO) that better constrain the abundances of the major species. A full inventory of molecules in the main planet-forming region (inside a few astronomical unit) provides important clues to the formation of even more complex molecules that eventually link back to the early history of our own solar system, the origin and delivery of water on Earth, and, eventually, the emergence of life. In addition, we follow the evolution of detailed dust mineralogy enabled by the unprecedented high signal-to-noise ratio (S/N) in the spectra. Such a comprehensive inventory of dust properties and gas composition also helps to understand the compositional dichotomy of the inner disk between disks around very low-

mass and solar-type stars first noted by Pascucci et al. (2009, 2013) based on Spitzer data.

1.1.2. Disk Dispersal

A series of atomic (neutral and ionized) and molecular lines as well as PAH and silicate features in the MIRI wavelength range will be used to determine the vertical structure of the disk surface layers and the presence of disk winds (e.g., [Ne II], [Fe II], [S I], H₂). These tracers test different scenarios for inner disk evolution and clearing such as internal photoevaporation, winds, dust settling/growth and planetesimal formation (e.g., Lahuis et al. 2007; Nomura et al. 2007; Pascucci et al. 2007; van Boekel et al. 2009; Baldovin-Saavedra et al. 2012; Sacco et al. 2012) as well as gas dispersal through accretion (see e.g., Manara et al. 2023). Indeed, the MIRI wavelength range covers many hydrogen recombination lines, which can be used to estimate mass accretion rates (e.g., Rigliaco et al. 2015; Franceschi et al. 2024).

We will also characterize the evolving gas composition well into the debris disk phase. The mid-IR traces ionized and atomic fine structure lines of sulfur, iron and molecular lines of SiO that are key in characterizing the nature of the gas and its link to planet formation (e.g., Gorti & Hollenbach 2004). The trace amounts of gas are often attributed to planetesimal collisions and/or collisions of terrestrial mass objects (e.g., Lisse et al. 2009; Dent et al. 2014). Depending on the gas temperature and the CO/H₂ ratio we may be able to discover molecular hydrogen emission from young debris disks.

1.1.3. Disk Structure in the Mid-IR

VLT/NACO, VLT/SPHERE, GPI and ALMA images show frequently inner depleted regions in disks as well as substructures such as bright secondary rims, azimuthal asymmetries, and/or spiral density waves (see Bae et al. 2023; Benisty et al. 2023, for recent PP VII chapters). Such features could be linked to forming massive planets. MIRI imaging not only provides the missing link between the scattered light by small micron-sized grains and thermal emission of mm-sized grains, but also has the capability of detecting massive protoplanets (Chen & Szulágyi 2022). We will eventually investigate whether and how disk substructure and pebble transport are linked to the diversity in chemical composition (Section 1.1.1).

2. Sample Selection

We selected our sample to contain young class II disks around stars of a wide range of spectral types in star-forming regions (Herbig Ae stars, T Tauri stars and very low-mass stars), and a sample of five young debris disks with CO sub-mm detections (e.g., 49 Ceti, HD 131835, HD 21997). Besides a few individual key targets (e.g., TW Hya, HD 169142,

PDS 70), we selected targets in the nearby (120–190 pc) Taurus, Ophiuchus, Chamaeleon and Lupus star-forming regions. After considering the MIRI/MRS brightness limits, the main selection criteria for our young class II disks were:

1. previous detection of molecular line emission and/or atomic fine structure lines with Spitzer (Najita et al. 2003; Pascucci et al. 2009, 2013; Pontoppidan et al. 2010; Salyk et al. 2011)
2. ground-based high spectral resolution CO rovibrational line profiles indicative of a disk origin (Najita et al. 2003; Salyk et al. 2009; Brown et al. 2013; Garufi et al. 2014; van der Plas et al. 2015)
3. some spread over the various star-forming regions, but the primary focus is on Taurus
4. existing (or scheduled) ALMA observations.

Our sample covers a stellar mass range 0.1–3 M_{\odot} (see Table 1): 5 Herbig disks (two of which close to edge-on), 33 T Tauri disks (four of which edge-on), 10 disks around very low-mass stars (VLMS,²⁸ one close to edge-on, 2MASS-J04381486+2611399).

For a few selected targets, we obtain additional NIRSpect IFU high-resolution spectroscopy: AA Tau (T Tauri), XX Cha (T Tauri), PDS 70 (T Tauri, see below), HK Tau B (T Tauri, edge-on), PDS 453 (T Tauri, edge-on), Flying Saucer (T Tauri, edge-on), HV Tau C (T Tauri, edge-on), and PDS 144 N (Herbig, edge-on). NIRSpect will provide additional information on key ice features and covers the main part of the CO rovibrational band. The observing strategy is detailed in Section 3.2.

Our targets with special signposts of planet formation are TW Hya, PDS 70, HD 135344B, and HD 169142. TW Hya is the closest known planet-forming disk at a distance of 60.14 pc (Gaia Collaboration et al. 2021) which shows rings in VLT/SPHERE and ALMA data down to au scales (Andrews et al. 2016; van Boekel et al. 2017). It is thus a prime target to search for signposts of protoplanets in thermal emission (Section 3.3). Another key target in this respect is PDS 70 with two gas giant protoplanets confirmed inside a dust gap (~ 17 –54 au, Keppler et al. 2018; Müller et al. 2018; Benisty et al. 2021, Section 3.4). HD 135344B is a disk around an F4V-type star with a dust cavity of ~ 40 au that shows intriguing rings and spiral structure in VLT/NACO and ALMA data (Garufi et al. 2013; van der Marel et al. 2016; Cazzoletti et al. 2018). Last but not least, the well-investigated planet-forming disk around the star HD 169142 is characterized by two gaps (e.g., Quanz et al. 2013) and an inner disk ($\lesssim 20$ au). Therefore, it shares some similarities with the PDS 70 system. The disk is very well spatially and kinematically characterized by VLT/SPHERE

²⁸ We use here a spectral type of M4 to distinguish between T Tauri and VLMS. However, this is not a well defined boundary and is used quite loosely in the literature.

Table 1
Overview of the JWST MINDS Disk Sample

Source	R.A. (ICRS) ep = 2015.5	Decl. (ICRS) ep = 2015.5	Region	Disk	SpT	d (pc)	T_{eff} (K)	L_* (L_{\odot})	M_* (M_{\odot})	$\log g$ ($\log(\text{cm s}^{-2})$)	[Fe/H]	ALMA/ SpitzerHR
49Cet (2)	01:34:37.88	-15:40:35.0	Argus Moving Group	D	A1	58.26	8770	15.58	1.99	4.18	-0.91	AS
CX-Tau (1)	04:14:47.87	+26:48:10.7	Taurus	TT	M1.5	126.74*	3487	0.34	0.33			AS
CY-Tau (1)	04:17:33.74	+28:20:46.4	Taurus	TT	M1.5	124.35	3516	0.37	0.35	3.99	0.17	AS
BP-Tau (1)	04:19:15.84	+29:06:26.5	Taurus	TT	K5/7	128.28	3777	0.83	0.47	4.21	-4.15	AS
FT-Tau (1)	04:23:39.20	+24:56:13.9	Taurus	TT	M2.8	129.96	3415	0.44	0.29	4.32	-4.15	AS
DF-Tau (1)	04:27:02.80	+25:42:22.0	Taurus	TT	M3	176.45*	3900	3.89	0.61			AS
DG-Tau (1)	04:27:04.70	+26:06:15.7	Taurus	TT	K6	130.21	4060	2.4	0.84	4.17	-1.49	AS
HH30	04:31:37.47	+18:12:24.5	Taurus	TTe	K7							A
HK-Tau-B	04:31:50.58	+24:24:16.4	Taurus	TTe	M0.5	128.53*						AS
DL-Tau (1)	04:33:39.09	+25:20:37.8	Taurus	TT	K7	159.53	4276	1.47	0.89	4.23	-2.49	AS
DM-Tau (1)	04:33:48.75	+18:10:09.7	Taurus	TT	M2	144.8	3415	0.25	0.29	4.06	-0.21	AS
AA-Tau (1)	04:34:55.43	+24:28:52.7	Taurus	TT	K5	137.72	3762	0.72	0.47	4.63	-3.91	AS
DN-Tau (1)	04:35:27.38	+24:14:58.6	Taurus	TT	M1:	127.29	3806	0.69	0.5	4.14	-4.07	AS
2MASS-J04381486+2611399 (1)	04:38:14.89	+26:11:39.6	Taurus	VLMSe	M7	140.26*	2840	0.003	0.06			AS
HV-Tau-C	04:38:35.51	+26:10:41.3	Taurus	TTe	M1							A
2MASS-J04390163+2336029 (1)	04:39:01.64	+23:36:02.6	Taurus	VLMS	M6	125.89	3139	0.1	0.17	4.22	0.16	AS
2MASS-J04390396+2544264 (1)	04:39:03.97	+25:44:26.0	Taurus	VLMS	M7	140.97*	2840	0.03	0.06			AS
LkCa15 (1)	04:39:17.80	+22:21:03.1	Taurus	TT	K5	154.83	4276	1.12	0.91	4.13	-0.34	AS
DR-Tau (1)	04:47:06.22	+16:58:42.6	Taurus	TT	K5	186.98	4202	3.71	1.11	4.09	-4.14	AS
HD32297	05:02:27.44	+07:27:39.3		D	A0	132.41	11250	24.42		4.5	-0.66	AS
RW-Aur	05:07:49.57	+30:24:04.9	Taurus	TT	K1/5+K5	150*						AS
HD35929	05:27:42.79	-08:19:38.5		H	F2	380.36*						AS
SY-Cha (1)	10:56:30.28	-77:11:39.4	Chamaeleon	TT	K5	180.78	4060	0.43	0.85	4.21	-1.14	AS
TW-Hya (1)	11:01:51.82	-34:42:17.2	TW Hya Moving Group	TT	K6	59.96	4000	0.34	0.75	4.05	-0.51	AS
2MASS-J11071668-7735532	11:07:16.56	-77:35:53.2	Chamaeleon	VLMS	M7.5/8	199.14	2664	0.04		3.78	0.79	
2MASS-J11071860-7732516 (1)	11:07:18.46	-77:32:51.6	Chamaeleon	VLMS	M5.5	197.52*	3060	0.03	0.13			A
2MASS-J11074245-7733593 (1)	11:07:42.34	-77:33:59.4	Chamaeleon	VLMS			3060	0.04	0.13			A
VW-Cha (1)	11:08:01.33	-77:42:28.6	Chamaeleon	TT	K7+M0	188.16*	4060	1.62	0.75			AS
2MASS-J11082650-7715550 (1)	11:08:26.37	-77:15:55.1	Chamaeleon	VLMS	M5.75	195.78*	3060	0.11	0.01			A
2MASS-J11085090-7625135 (1)	11:08:50.81	-76:25:13.7	Chamaeleon	VLMS	M4	192.24*	3060	0.03	0.13			A
WX-Cha	11:09:58.57	-77:37:09.0	Chamaeleon	TT	M1+M5							AS
XX-Cha (1)	11:11:39.58	-76:20:15.0	Chamaeleon	TT	M3	194.64	3340	0.29	0.25	4.5	-1.18	AS
Sz50	13:00:55.24	-77:10:22.4	Chamaeleon	TT	M3							AS
PDS70	14:08:10.11	-41:23:52.9	Upper Centaurus Lupus	TT	K7	112.32	4138	0.38		4.15	0.11	A
HD131835	14:56:54.44	-35:41:44.1	Upper Centaurus Lupus	D	A2	130.28	8408	10.39	1.77	4.23	-0.6	A
HD135344B (2)	15:15:48.42	-37:09:16.4	Upper Centaurus Lupus	H	F8	135.41	6620	7.07	1.58	3.8	-0.82	AS
HD138813	15:35:16.08	-25:44:03.4	Upper Scorpius	D	A0	136.42	9900	26.88	2.23	4.14	-1.42	AS
GW-Lup (1)	15:46:44.71	-34:30:36.0	Lupus	TT	M1.5	155.20*	3632	0.33	0.41			AS
PDS144N	15:49:15.55	-26:00:49.6		He	A2	130.00*						S
IM-Lup (1)	15:56:09.19	-37:56:06.5	Lupus	TT	M0	153.81	4350	2.57	0.95	4.06	-0.39	AS
2MASS-J15582981-2310077 (1)	15:58:29.80	-23:10:08.1	Upper Scorpius	TT	M3	136.81	3388	0.05	0.31	4.56	0.49	AS
2MASS-J16053215-1933159 (1)	16:05:32.14	-19:33:16.3	Upper Scorpius	VLMS	M5	158.17	3090	0.03	0.13	3.91	-0.5	AS
Sz98 (1)	16:08:22.48	-39:04:46.8	Lupus	TT	M0.4	156.27*	4060	1.51	0.67			A

Table 1
(Continued)

Source	R.A. (ICRS) ep = 2015.5	Decl. (ICRS) ep = 2015.5	Region	Disk	SpT	d (pc)	T_{eff} (K)	L_* (L_{\odot})	M_* (M_{\odot})	$\log g$ ($\log(\text{cm s}^{-2})$)	[Fe/H]	ALMA/ SpitzerHR
V1094Sco (1)	16:08:36.16	−39:23:02.8	Lupus	TT	K6/K5	152.44	4205	1.15	0.83	4.17	−0.7	A
SR21	16:27:10.27	−24:19:13.1	Ophiucus	TT	G1	136.43*						AS
IRS46	16:27:29.42	−24:39:16.6	Ophiucus	TT								AS
2MASS-J16281370-2431391	16:28:13.75	−24:31:40.0	Ophiucus	TTe								A
RNO90	16:34:09.16	−15:48:17.2	Ophiucus	TT	G5	114.96*						AS
WA-Oph6	16:48:45.62	−14:16:36.2	Ophiucus	TT		122.53*						AS
PDS453	17:20:56.12	−26:03:31.0		He	F2	129.05*						
HD169142	18:24:29.78	−29:46:49.9		H	F1	115.36	7209	6.21	1.51	4.12	−1.88	AS
HD172555	18:45:26.98	−64:52:18.9	β Pic Moving Group	D	A7	28.78*						AS

Note. Coordinates are taken from Gaia DR2, effective temperature T_{eff} , stellar luminosity L_* and stellar mass M_* come either from (1) Testi et al. (2022), (2) Kaeufer et al. (2023), or Gaia DR3; distance d , $\log g$ and [Fe/H] are retrieved from Gaia DR3. Spectral types (SpT) are collected from Simbad. The last column denotes the existence of either ALMA observations (A), Spitzer-IRS High resolution data (S), or both (AS). Disk types are defined as follows: T Tauri disk (TT); Debris disk (D); Herbig disk (H); very low-mass star disk (VLMS); edge-on disk (extra letter “e” appended). A “*” symbol in the distance column means that it has been estimated from the parallax.

and ALMA observations and an earlier claimed detection of a protoplanet at 37 au (Gratton et al. 2019) is now confirmed by re-analyzing VLT/SPHERE data (Hammond et al. 2023).

3. Observing Strategy

We detail here our observing strategy for the MIRI (Wells et al. 2015; Wright et al. 2015, 2023; Labiano et al. 2021), NIRSpec (Jakobsen et al. 2022) and NIRCам (Burriesci 2005; Rieke et al. 2005) observations of our MINDS survey. At this stage, all sources listed in Table 1 have been observed (MIRI/MRS, NIRSpec/IFU, NIRCам imaging and MIRI coronagraphy) except for the MIRI/MRS observation of SR 21 and J04390396+2544264, the NIRSpec observation of the flying saucer and the MIRI/MRS and coronagraphic observations of HD 163296. The published data products will be made available to the community via our website <https://minds.cab.inta-csic.es>.

3.1. MIRI/MRS Spectroscopy

We use MIRI/MRS ($R \sim 3000$) and cover the entire wavelength range (all four channels) with S/N values of 100–500 on the continuum. We apply a 4-point point-source dither pattern and typical exposure times between 1800 and 3600 s on source. For a few bright targets (DG Tau B, RNO 90, SR 21, PDS 144 N, HD 135344B), we use a non-standard choice of 3 groups to minimize saturation primarily in the short wavelength channels.

For sources that were identified as extended (DG Tau B, Flying Saucer, HH 30, HD 135344 B, TW Hya), we implement a dedicated background at a clean offset position. The integration time is equal to that in a single dither position. In those cases, we also use the 4-point extended-source dither pattern. We also added this for the two sources WX Cha and XX Cha which were scheduled at the beginning of JWST observations, so that we could assess the importance of a dedicated background for the quality of the data reduction. For other sources, we extract the background from the on-source IFU image (see Section 4.2).

Most of our targets are bright and we decided to go without a dedicated target acquisition (TA). For a few key sources where we expect very faint emission and/or search for disk substructures, we implemented TA using a neutral density filter (FND) and fast readout (FASTR1); MIRI/MRS observations of two targets, PDS 70 and HD 169142 are described in more detail below.

Since many of our sources belonging to the same star-forming region can be grouped, we benefit from shorter slew times, thus reducing the overheads (Smart Accounting).

3.2. NIRSpec/IFU Spectroscopy

We take high-resolution ($R \sim 2700$) spectra in the long wavelength channel of NIRSpec, G395H/L290LP, 2.87–5.27 μm for six sources: AA Tau, HK Tau B, PDS 453, XX Cha, PDS 70, and the Flying Saucer. Again, we skip TA and we use a 4-point-nod dither. With 600–700 s on source, we reach a S/N of a 100–200 for a 100 mJy (continuum) source.

3.3. MIRI Coronagraphy of TW Hya

Detailed coronagraphic simulations based on recent SPHERE images show that the best wavelength for detecting disk substructure is 15.5 μm (E. Pantin 2024, private communication). This wavelength is also better suited for giant planet detection because it avoids the strong silicate band emission originating from dust in the inner disk. In 1800 s, we reach a sensitivity of $\sim 5 \mu\text{Jy}/10\sigma$. We take two position angles (10° – 14° difference) and also use a comparison star for point-spread function (PSF) subtraction, 26 Crt. Calibration background sequences have been added in order to suppress the thermal background straylight discovered during MIRI commissioning (Boccaletti et al. 2022).

3.4. A Pan-instrument View of PDS70

We decided to study this iconic system hosting two gas giant protoplanets with three different instruments onboard JWST to characterize (i) the warm gas and dust composition/sizes in the inner disk (MIRI/NIRSpec IFU spectroscopy), (ii) the protoplanet properties (NIRCам direct imaging) and to (iii) try to detect the circumplanetary disks around the protoplanets (MIRI/NIRCам).

MIRI and NIRSpec IFU spectroscopy are implemented in the same way as for the other objects in our sample. The main difference is that we do TA with MIRI to ensure an optimum fringe correction, and that we integrate deeper, ~ 1 hr on source (~ 63 minutes with MIRI and ~ 77 minutes with NIRSpec). The NIRSpec data will give us access to the full CO rovibrational band (contrary to MIRI).

NIRCам imaging is performed in two filters, F187N and F480M. To avoid saturation in direct imaging, we use the subarray SUB64P (64×64 pixels corresponding to $2'' \times 2''$) to allow fast readout (RAPID). We use two position angles (PA1 and PA2), separated by 5° (the maximum possible to avoid scheduling issues) and for each of them 142 integrations each with 7 groups, resulting in a total exposure time of ~ 5 minutes per PA. The primary filter F187N is chosen to detect the protoplanets thermal emission; it also covers Pa α , a tracer of gas accretion onto a forming gas giant planet (Aoyama et al. 2018). We aim to use the “free” extra filter F480M to search for CO rovibrational emission, which could be due to the presence of a circumplanetary disk (Oberg et al. 2023).

3.5. Characterizing the HD 169142 Inner Disk and Protoplanet

We will obtain MIRI/MRS data for this source in the same way as for our T Tauri disks. The difference is that we will obtain in a single observing sequence both coronagraphic imaging and MIRI/MRS observations (PID 4525). This choice is motivated to image and potentially spectrally characterize the CPD of the protoplanet, in addition to constraining the chemistry of the inner disk. The coronagraphic observation is a 36 minutes integration with the 4-quadrant phase-mask at $10.65\ \mu\text{m}$, using fast readout mode and a 9-point small grid dither; we use a PSF reference star and a dedicated background observation as recommended in Boccaletti et al. (2022). For MIRI/MRS observations, we use a short 5 minutes exposure to avoid saturation and a 4-point extended-source dither and dedicated TA using the F1500W filter. This data can be used to study spatially extended mid-IR emission as well as the mid-IR spectrum.

3.6. A Serendipitous Search for Asteroids

MIRI/MRS observations allow for parallel imaging at no extra cost (except the data volume rate), so-called “simultaneous imaging.” Since our targets are all close to the ecliptic, we decided to implement a parallel imaging program focusing on the search for asteroids. Based on the expected typical temperatures, we adopted the F1280W filter for that serendipitous science goal. The integrations and groups for the imager are adjusted so that the total integration time is smaller but as close as possible to the main MIRI/MRS observations. The field of view of the parallel images is $74'' \times 113''$. We implement this for all our targets except in cases where we exceed the allowed data volume (data excess $>15,000$ MB).

4. Data Reduction

We describe in this section the global procedure adopted for the reduction of our MIRI/MRS MINDS data, highlighting the choices made for the TW Hya data set. For the reduction of our data acquired with a different JWST instrument or different MIRI observing mode (i.e., NIRSpec/IFU, MIRI coronagraphy and NIRCAM imaging), we refer the interested reader to our upcoming papers presenting the respective data sets.

4.1. Standard Pipeline

The MIRI/MRS MINDS data are processed from the uncalibrated raw data files using the JWST pipeline (version 1.12.5, Bushouse et al. 2022, for TW Hya) and Calibration Reference Data System context (`jwst_1146.pmap` for TW Hya). A stray light correction is applied with the standard pipeline to remove contamination produced by internal reflections within the MIRI detector arrays. Our reduction procedure was complemented with routines from the VIP

package (Gomez Gonzalez et al. 2017; Christiaens et al. 2023), used in particular for enhanced bad pixel correction (performed after stage 2, yielding less spikes in the final spectra), and source centroid identification for faint targets (Section 4.4).

4.2. Background Subtraction

To remove the background in the absence of dedicated background observations, we considered three options, the first two operate on the rate-files at the detector stage (i.e., as for the subtraction of dedicated background images), the last on the built spectral cubes: (a) carry out a direct pair-wise dither subtraction, (b) leverage the four-point dither pattern to obtain a first guess on the background map, then refine it using a median-filter which both smooths the background estimate and removes residual star signals from it, or (c) estimate the background in an annulus directly surrounding the aperture used for photometry extraction. In general, the annulus background subtraction was the most robust and provides consistently good results without introducing extra noise. For faint targets it is worth trying a combination of (b) with a small aperture to minimize the impact of artifacts introduced by using the dithers for building a subtraction template. For data sets where dedicated background observations are available, such as TW Hya, we also tried to subtract the dedicated background frames on the detector level. However, due to their limited exposure time compared to the science sequence, they introduce more noise than when performing an annulus subtraction in the extracted image cube. Hence, spectra shown in this work make use of the annulus subtraction approach.

4.3. Fringe Correction

We apply three fringe corrections to the data: the standard fringe flat correction (`flat_field`) that takes place in stage 2 of the pipeline, a residual fringe correction (`residual_fringe_step`) between stages 2 and 3 (Argyriou et al. 2020), and a spectrum-level fringe correction after stage 3 (P. J. Kavanagh et al. 2024, in preparation). The final spectrum-level fringe correction is done on individual sub-bands, extracted from stage 3, to avoid any residuals that may be produced by stitching sub-bands together. For sources with TA, we perform fringe removal using the calibration files provided by Gasman et al. (2023). Since most of our targets are taken without TA, using the asteroid observations for fringe correction as done in Pontoppidan et al. (2024) is not straightforward.

4.4. Spectrum Extraction

The MIRI Medium Resolution Spectroscopy (MRS) mode is characterized by four channels, covering the $4.9\text{--}27.9\ \mu\text{m}$ spectral range. Each channel has three sub-bands, SHORT (A), MEDIUM (B) and LONG (C) resulting in a full spectrum composed by twelve sub-bands (Wells et al. 2015). The

spectral resolving power changes from $R = 3100\text{--}3750$ (channel 1, $4.9\text{--}7.65\ \mu\text{m}$) to $R = 1330\text{--}1930$ (channel 4, $17.7\text{--}27.9\ \mu\text{m}$). The spectrum is extracted on source using an aperture of 2 FWHM (2 times $1.22 \times \lambda/D$) by default, with the centroid of the source identified through a Gaussian fit in a weighted average image for each sub-band. This is different from (Pontoppidan et al. 2024), who use 2.8 FWHM. Generally, the wavelength calibration is accurate to better than ~ 1 spectral resolution element ($\sim 10\text{--}30\ \text{km s}^{-1}$; Argyriou et al. 2023).

5. Modeling Approach

For the qualitative and quantitative analysis and interpretation of the JWST data, we use a range of models with different levels of complexity, ranging from 0D slab models to full 2D radiation thermo-chemical disk models (for details see also Kamp et al. 2023). Fast retrieval for molecular emission features is done with 0D slab models, while grids or series of 2D radiative transfer and/or thermo-chemical models allow us to assess the impact of certain physical parameters on the disk spectra and images in a forward modeling manner. Below, we describe the various models in more detail.

5.1. Slab Models

For the fast retrieval, we use 0D slab models calculated with either an in-house LTE slab model (Tabone et al. 2023, see also Grant et al. 2023 or Perotti et al. 2023), the ProDiMo (Thi et al. 2013; Woitke et al. 2016), or the RADEX code (van der Tak et al. 2007). Slab models are generally run for each molecular species separately. The slab models assume a homogeneous medium with a constant gas temperature T_{gas} and species density. Multiple collision partners (e.g., H, H_2 , He, e^-) and their corresponding densities n_c can be specified. In addition, we can include IR pumping, for example from thermal dust emission. The level populations are solved either in LTE (using pre-tabulated partition functions from HITRAN2020, Gordon et al. 2022) or non-LTE (Song et al. 2015; Ramírez-Tannus et al. 2023). The models use a simple 1D radiative transfer (plane-parallel slab geometry) to calculate the emergent intensity from a slab with a species column density N_{sp} . For very high column densities, line-overlap between lines of a specific molecule can become important. We treat this assuming a combination of thermal and turbulent broadening (e.g., Tabone et al. 2023).

An overview of the molecular data used for calculating the mid-IR spectra is shown in Table 2. In some cases, collision cross sections exist and have been compiled, e.g., for CO, CO_2 , OH, and HCN. In those cases non-LTE effects have been investigated and quantified; the respective references listed in the table contain more detailed information.

Such 0D slab models are computationally inexpensive and we can run large grids for each molecule and isotopologue. For

Table 2
Molecules with Emission in the Mid-IR Spectral Region used in the 0D Slab Models and Thermo-chemical Disk Models

Molecule	Treatment	# Levels	# Lines	References
o- H_2O	non-LTE	411	7597	LAMDA
p- H_2O	non-LTE	413	7341	LAMDA
OH	non-LTE	412	2360	Tabone et al. (2021) ^a
OH (1)	LTE		56905	HITRAN2020
O_2 (1)	LTE		29793	HITRAN2020
CO	non-LTE	300	1470	Thi et al. (2013), Song et al. (2015) ^b
CO_2	non-LTE	640	3698	Bosman et al. (2017)
$^{13}\text{CO}_2$	non-LTE	640	3387	Bosman et al. (2017)
CO_2 (1)	LTE		539603	HITRAN2020
H_2CO (1)	LTE		44601	HITRAN2020
CH_4 (1)	LTE		445749	HITRAN2020
C_2H_2 (1)	LTE		83967	HITRAN2020
C_2H_4 (1)	LTE		77631	HITRAN2020
C_2H_6 (1)	LTE		70623	HITRAN2020
C_3H_4	LTE		9906	Arabhavi et al. (2024, submitted)
C_4H_2	LTE		251245	HITRAN2020
C_6H_6	LTE		54608	Arabhavi et al. (2024, submitted)
CH_3OH	LTE		19897	HITRAN2020
NH_3 (1)	LTE		90396	HITRAN2020
NO (1)	LTE		384305	HITRAN2020
N_2O (1)	LTE		160478	HITRAN2020
HCN	non-LTE	602	4622	Bruderer et al. (2015)
HCN (1)	LTE		151484	HITRAN2020
HC_3N	LTE		248273	HITRAN2020
CH_3CN	LTE		3572	HITRAN2020
H_2S (1)	LTE		54228	HITRAN2020
SO (1)	LTE		44264	HITRAN2020
SO_2 (1)	LTE		975058	HITRAN2020
SO_3	LTE		14295	HITRAN2020
CS (1)	LTE		2078	HITRAN2020
OCS (1)	LTE		37461	HITRAN2020
CH_3^+	LTE		16200	Changala et al. (2023)

Notes. Molecules for which we have isotopologue data are denoted by a (1) behind the molecule. For LTE treatment, we only list the number of lines.

^a A sub-selection has been made for the two lowest vibrational levels, $v = 0$ and $v = 1$.

^b A sub-selection has been made for up to $v = 5$ and $J = 60$ in each vibrational level of the ground electronic state.

the retrieval part of our project, we use a refined χ^2 minimalization approach. Grids of selected molecular 0D slab models as well as the modeling software (python) are made available to the community in Arabhavi et al. (2024, submitted). In order to provide an optimal result, the fitting procedure has to be constrained to relatively small wavelength ranges per molecule; ideally those ranges are free of emission from other molecules. Since this is often hard to find, we also use an iterative approach. We first fit the molecule being the strongest contributor to the line emission, then we subtract that best fit spectrum and proceed to the next molecule. In this way,

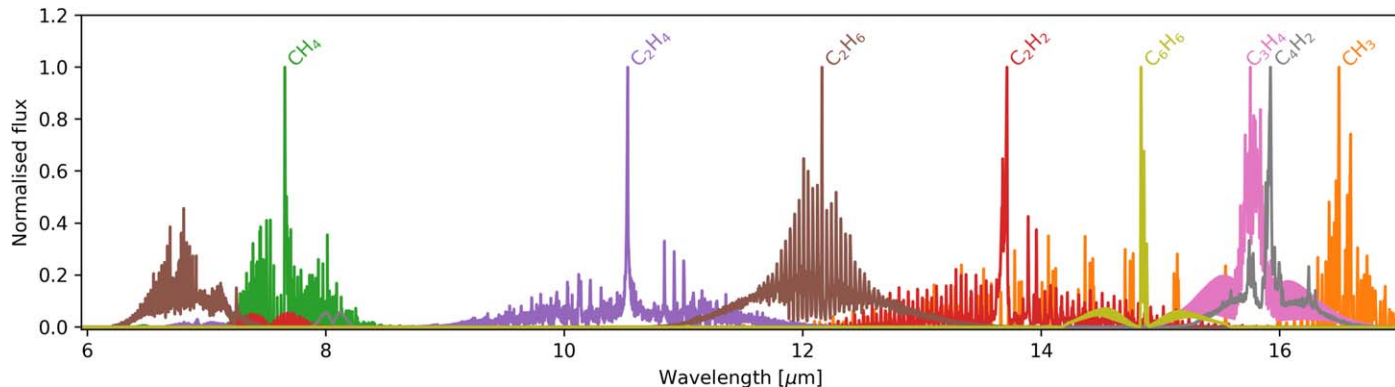


Figure 1. ProDiMo LTE slab models with a series of hydrocarbons from the HITRAN2020 database (Gordon et al. 2022) and from Arabhavi et al. (2024, submitted); line strengths have been normalized to the strongest intensity.

we can successively proceed from the strongest to the weakest emission (see e.g., Grant et al. 2023; Schwarz et al. 2024).

For specific molecules which have lines distributed over the full MIRI wavelength range, it can be impossible to fit the emission at all wavelengths with a single set of 0D slab model parameters. This has been noted already for water in Spitzer spectra (Liu et al. 2019; James et al. 2022), but was hard to quantify due to the strong blending of lines at a resolution of $R \sim 600$. With the increased spectral resolution of MIRI, we find now clear evidence for radial temperature gradients from fitting 0D slab models to a series of wavelength intervals (e.g., Gasman et al. 2023).

Given the higher sensitivity and spectral resolution of JWST/MIRI, we expect to see higher excitation weaker bands (mostly Q-branches of overtones or combination bands) as well as isotopologues (see for the example of CO_2 , Bosman et al. 2018, 2022b). The mid-IR is also very rich in more complex hydrocarbons that could have lower abundances than C_2H_2 , but still be detectable mainly through their pronounced Q-branches (Figure 1).

5.2. Simple Two-component Disk Models

The molecular emission, continuum and dust solid-state features are sometimes difficult to disentangle. In those cases, we employ simplified disk models, that account for realistic dust opacities, radial temperature gradients and capture the two-layer nature of massive planet-forming disks. Examples hereof are dust retrieval tools following the approach of Juhász et al. (2009) and the CLICk tool for fitting spectra in the presence of quasi-continua from blended line emission on top of dust continua (Liu et al. 2019).

The two-layer disk models calculate the continuum emission from annuli in an optically thick midplane emitting as a blackbody with a radial temperature gradient and an optically thin atmosphere (surface) which gives rise to the solid-state emission bands. The optically thick part can also contain a

puffed up inner rim component. Molecular emission has been included in such two-layer models by assuming that the surface layer itself is optically thin in the continuum, i.e., the molecular emission at mid-IR wavelengths is not attenuated by dust.

We evaluate the opacities of a number of minerals using DHS (Min et al. 2005) and a transmission absorption spectrum for diopside. The optical constants are taken from Zeidler et al. (2015, enstatite), Suto et al. (2006, forsterite), Koike & Shibai (1990, hydrosilicates), Koike et al. (2000, diopside, see also Posch et al. 2007). Figure 2 shows that high S/N spectra in the MIRI wavelength range give unique access to rare dust species such as hydrous minerals (montmorillonite, serpentine) and calcite. These are minor constituents of meteorites in the solar system (Suttle et al. 2021).

5.3. 2D/3D Disk Models

The SEDs of optically thin debris disks are modeled using the SONATA code (Pawellek & Krivov 2015). For modeling debris disk images (e.g., MIRI IFU data) the 3D code MODERATO is used (Pawellek et al. 2024). Optically thick planet-forming disks are modeled using Monte-Carlo radiative transfer codes such as RADMC-3D (Dullemond et al. 2012), MCMAX-3D (Min et al. 2009), or 2D thermo-chemical disk codes such as DALI (Bruderer et al. 2012) and ProDiMo (Woitke et al. 2009, 2016; Kamp et al. 2010; Thi et al. 2011).

Since the focus of the MINDS program is the gas emission, we describe here briefly the power and drawbacks of thermo-chemical disk codes in some more detail. For details on the code structure, specific features and typical model set-ups, we refer to the respective papers of DALI and ProDiMo above.

The typical runtime of a full thermo-chemical model is of the order of a few hours to a day (depending on the grid resolution, size of chemical network). This makes it immediately clear that such models cannot be used in straightforward Bayesian retrievals. In a fully consistent thermo-chemical model, the dust and gas structure are coupled through the radiative transfer and

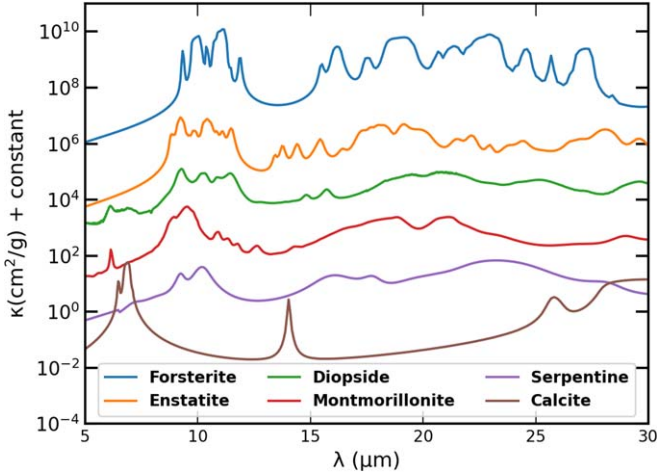


Figure 2. Opacities of various key minerals showing the richness of the MIRI wavelength range, especially the potential to detect rare minerals such as diopside, montmorillonite, serpentine and calcite.

the chemistry; hence the abundances of atoms, ions and molecular species are constrained by the disk structure and assumptions on the dust properties. The same is true for the gas temperature, which is a result of the heating/cooling balance (which depends on species abundances). Dust settling and its treatment plays a key role as it determines the degree to which large grains settle and hence the dust opacity in the surface layers that we can observe with MIRI. DALI and ProDiMo use different approaches. DALI uses typically two grain components, a small and a large one, where the latter is settled to a lower scale height (free parameter). ProDiMo allows also for a parametrized settling, but most often uses the settling model by Dubrulle (Dubrulle et al. 1995, see also Schr apler & Henning 2004) or Riols settling (Riols & Lesur 2018). The former settles the dust grains according to the midplane sound speed, while the latter uses the local sound speed (Woitke et al. 2024). In the past, ad-hoc assumptions on molecular abundances, gas-to-dust ratios and/or gas temperatures have been employed to match mid-IR molecular emission spectra from disks. However, a wealth of studies over the past decade has improved our understanding of how the mid-IR molecular emission depends on inner disk structure, dust evolution, molecular shielding, dust opacities, gas temperatures, and element abundances (e.g., Bethell & Bergin 2009; Antonellini et al. 2015; Woitke et al. 2018, 2019; Greenwood et al. 2019; Anderson et al. 2021; Bosman et al. 2022a, 2022b; Kamp et al. 2023). Taking into account as much of these improvement as possible, Woitke et al. (2024) were able to capture the key features of the MIRI spectrum of EX Lup (K osp al et al. 2023) with a thermo-chemical disk model using ProDiMo.

Due to the sheer number of lines and line density in the near- and mid-IR, an important component for predicting JWST spectra is a fast line radiative transfer. This led to the

development of standalone codes such as RADLite (Pontoppidan et al. 2009) and FLiTs (Woitke et al. 2018), which generally take the density, abundance and temperature structures from an external 2D disk code. Both line radiative transfer codes take into account the large velocity gradients across grid cells in the inner disk as well as the dust opacity. FLiTs also accounts consistently for opacity overlap between lines; this can be important for the Q-branches of species such as CO₂, HCN, C₂H₂ (also with their respective isotopologues) and OH/water (Pontoppidan et al. 2009; Woitke et al. 2018). Within the thermo-chemical codes, modules have been added to allow approximative calculation of realistic mid-IR emission spectra (e.g., for DALI, Bosman et al. 2017).

Such forward models include the complex interplay between gas and dust in realistic disk geometries benchmarked against a large range of multi-wavelength observations (e.g., Woitke et al. 2019). It is hence tempting to use these models to predict where the new discovery space for JWST is. In this way, Bosman et al. (2017) showed the diagnostic power of detecting the rarer isotopologue ¹³CO₂ and Woitke et al. (2018) showed how multiple species can be used to determine the C/O ratio in disks (see also Anderson et al. 2021). The models can also be used to generate a testbed for retrieval codes (such as the slab models and CLiC introduced above). Figure 3 shows the predicted mid-IR spectrum for the DIANA SED model of AA Tau.²⁹ We used here a gas-to-dust ratio of 1000 and a selection of the molecular data listed in Table 2. The disk model is re-calculated with ProDiMo, using the large DIANA chemical network (Kamp et al. 2017). We then post-process the results with FLiTs to generate a mid-IR spectrum with a resolution of 30,000. We add a typical noise level of 300 (representative for what MINDS aims at for T Tauri disks) and sample with a constant resolution of 3000 (oversample = 2). The model spectrum matches well the Spitzer IRS high resolution spectrum (Figure 3); the continuum flux offset at 15 μ m is only 0.05 Jy. It is clear that we need high S/N MIRI spectra (S/N \gg 200) to be able to reveal for example the weak R- and P-branch lines in the CO₂ spectrum.

6. First Results

We present here a brief summary of the first results from MINDS, before focusing on one specific object, TW Hya, in more detail.

6.1. Early MINDS Results

Within the MINDS program we have presently observed more than 30 T Tauri stars with different disk sizes and masses and a variety of disk substructures (see Table 1). This will allow us to constrain statistically for example the dependence

²⁹ DIANA models are publically available from <https://prodimo.iwf.oaw.ac.at/models>.

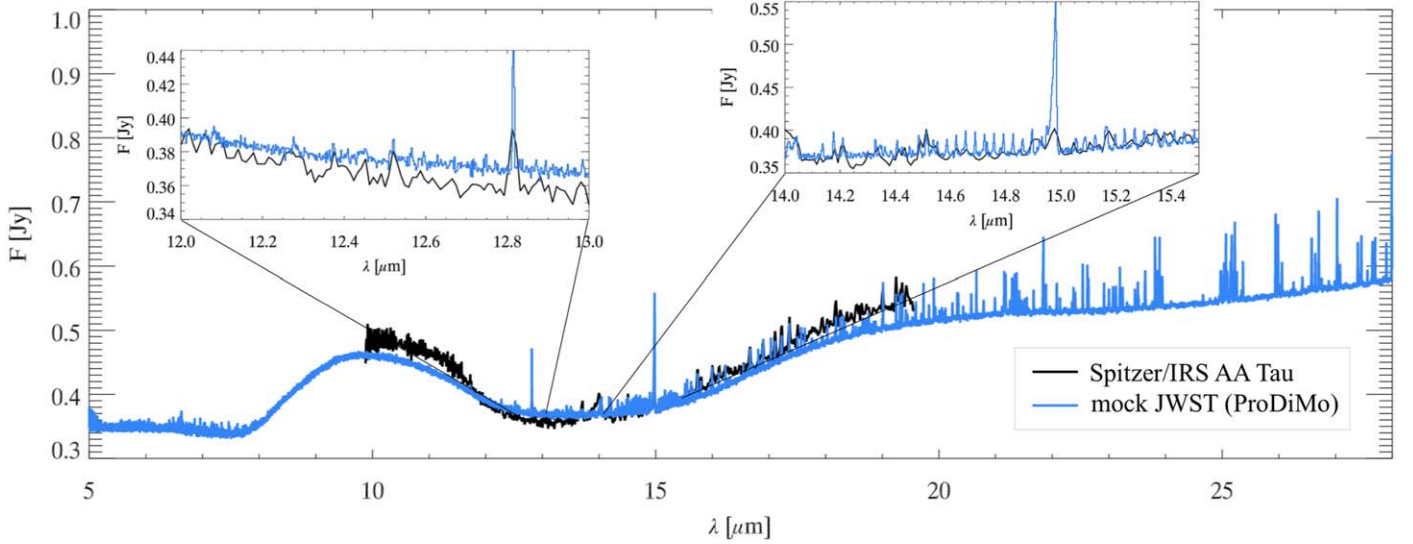


Figure 3. Simulated mid-IR spectrum ($R = 3000$) for the disk around the star AA Tau including the full suite of atomic, ionic and molecular cooling lines (blue, DIANA SED model, $S/N = 300$, $\sigma = 2$ mJy). The Spitzer high resolution IRS spectrum ($R \sim 600$) is shown in black (shifted by +50 mJy). The two insets cover the region of H_2O and $[Ne II]$ at $12.8 \mu m$ and the CO_2 region at $15 \mu m$.

of the water distribution as a function of disk properties. In the disk around the T Tauri star GW Lup, we discovered the molecular emission from CO, H_2O , OH, CO_2 , and HCN (Grant et al. 2023). For the first time, we could also detect the $^{13}CO_2$ isotopologue in a disk. We derived a surprisingly high ratio of CO_2 -to- H_2O column density of ~ 0.7 . This high ratio may be caused by an inner cavity between the H_2O and CO_2 mid-plane snowlines, blocking the transport of water-ice rich pebbles (Vlasblom et al. 2024). Another example of the MINDS program is the observation of the T Tauri star Sz 98 with its unusually large dust disk (Gasman et al. 2023). Despite the presence of such a large disk, we find abundant water emission in the inner disk, pointing to a subsolar C/O ratio. This is in strong contrast to the outer disk where a C/O ratio larger than unity was measured with ALMA (Miotello et al. 2019). A MINDS study by Perotti et al. (2023) found water in the very inner disk of the young planetary system PDS 70. The water molecules can be both self-shielded and protected by the presence of small micron-sized dust particles. The water reservoir could be formed in situ in the inner disk or be sustained by water-rich dust particles transported from the outer disk. These scenarios are not exclusive and plausibly both contribute. The two planets and evidence for accretion flows have been discovered in the MINDS NIRCAM images of PDS 70 (Christiaens et al. 2024).

The MINDS sample contains also a number of disks around very low-mass M-type stars dwarfs. In the disk around such a low-mass star (J16053215) the emission of a variety of hydrocarbons, including benzene was found (Tabone et al. 2023). Strong broad bumps at 7.7 and $13.7 \mu m$ are due to

optically thick C_2H_2 emission. Its column densities are a factor ~ 1000 higher than in other disks leading to a pseudo-continuum. The JWST observations of this source show a complete lack of silicate emission features, indicating that the grains are settled toward the mid-plane or grown to larger than a few micron. The hydrocarbon chemistry points to a large C/O ratio in the inner 0.1 au of this disk (Kanwar et al. 2024, Kanwar et al. 2024, submitted). A possible hypothesis is that oxygen is locked-up in icy pebbles and planetesimals outside of the water ice-line. Another possibility is the faster transport of pebbles covered by water ice causing most oxygen to have been accreted onto the star (Mah et al. 2023).

6.2. The Nearby Disk Around TW Hya

The TW Hya star-disk system has been intensively studied because of its proximity, accretion behavior, and disk structure. With a Gaia DR3 distance of only 60 pc (Gaia Collaboration et al. 2021), TW Hya is the nearest T Tauri star with a dusty gas-rich disk. It is a member of the TWA association with an age of 10 ± 2 Myr (Gaia DR3, Luhman 2023) in agreement with earlier age estimates (Hoff et al. 1998; Barrado Y Navascués 2006). Despite this age, the disk is still relatively massive ($\gtrsim 0.05 M_\odot$, Bergin et al. 2013; Franceschi et al. 2022). The system is seen nearly face-on (Qi et al. 2004) making it an excellent target for infrared spectroscopy of the disk. Zhang et al. (2013) found the Herschel and Spitzer water line detections to be consistent with the inner few astronomical unit of this system being depleted in water (factor of ~ 100). In a follow-up study Bosman & Banzatti (2019) combined archival Spitzer and VLT/CRIFES data and performed a detailed

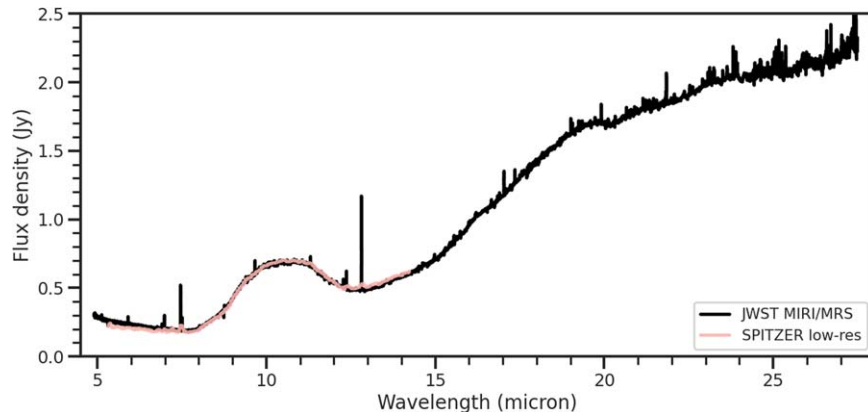


Figure 4. Comparison of JWST/MIRI and Spitzer low resolution spectrum of TW Hya (no scaling).

analysis with a thermochemical model. They concluded that the inner disk is not enriched by ice-covered inward drifting pebbles because the elemental carbon and oxygen abundances are about a factor of 50 smaller than in the interstellar medium (also in agreement with atomic line analysis by McClure et al. 2020). The authors proposed that the drifting pebbles are stopped in a dust trap outside the water ice line.

The disk around TW Hya is characterized by a system of rings and gaps with a high degree of azimuthal symmetry. Based on the analysis of the spectral energy distribution with its small near-infrared excess, the TW Hya disk has been classified as a “transition disk” with a characteristic radius of ~ 4 au separating optically thick submicron-sized grains and optically thin dust at smaller radii (Calvet et al. 2002). In scattered light near-infrared images tracing the distribution of submicron-sized particles, three radial gaps have been discovered (van Boekel et al. 2017). ALMA observations (Andrews et al. 2016; Tsukagoshi et al. 2016), revealing the spatial distribution of millimeter-sized dust grains, demonstrate the presence of a system of concentric ring-shaped substructures at the same position. Relevant for the MIRI observations of this disk, we note that the ALMA observations found evidence for the presence of a narrow dark annulus at 1 au. The rim of the innermost (optically thin) dusty disk is located at ~ 0.04 au from the source (Gravity Collaboration et al. 2020, 2023; GRAVITY Collaboration et al. 2021). A comprehensive analysis by Menu et al. (2014), combining mid-infrared interferometry data with submillimeter and eVLA observations provided a structural model of the inner disk regions consisting of a peak surface density at about 2.5 au, with a smooth decrease inwards to 0.35 au.

6.2.1. Analysis of the MIRI Spectrum

In Figure 4 we show the broad-wavelength MIRI spectrum between 4.9 and 27.9 μm and compare it with the Spitzer low-resolution spectrum. The small remaining absorption features

are not real and are expected to vanish with improvements in the data reduction pipeline. At variance with other sources of the sample (e.g., GW Lup, Sz 98, SY Cha; see Gasman et al. 2023; Grant et al. 2023; Schwarz et al. 2024), within the calibration uncertainties, we do not find any continuum flux difference between Spitzer and JWST up to 15 μm , nor a change in the silicate emission feature shape. We leave the study of potential line variability to future work. We define a continuum based on line-free regions and subtract this continuum to identify emission features in the spectrum. Figure 5 zooms into the spectrum and identifies the key lines and features.

Fine-structure lines: At wavelengths below 10 μm , we detect the [Ar II] emission line at 6.99 μm . The [Ar III] emission lines at 6.36, 8.99 and 21.82 μm are not detected. We also detect [Ne II] at 12.81 μm and [Ne III] at 15.56 μm (previously detected by Spitzer, Najita et al. 2010).

H₂ lines: The full series of H₂ lines from S(8) to S(3) is detected in addition to the previously reported S(2) and S(1) lines seen in Spitzer high resolution spectra (Najita et al. 2010).

HD lines: Several of the HD lines in the MIRI wavelength range are blended with water lines. The longer wavelength lines at 15.022 and 23.033 μm are not detected above the noise level. We find that the former one coincides with a CO₂ P-branch line and ruling out a detection with high confidence requires an accurate fitting of the CO₂ molecule emission.

OH and water: We detect OH emission longward of ~ 9 μm and water emission longward of 14 μm . The shortest water emission so far reported for TW Hya has been at 21.85 μm (Bosman & Banzatti 2019); we now clearly detect a number of water lines also in the 14–15 μm region (Figure 6(e)), but not the H₂O rovibrational lines at 6–7 μm . Between 9 and 10.5 μm , we see the clear signature of OH prompt emission (UV photodissociation of water populates only two of the four OH components, Tabone et al. 2021; Zannese et al. 2023). The OH quadruplets beyond 14 μm are more symmetric than those at

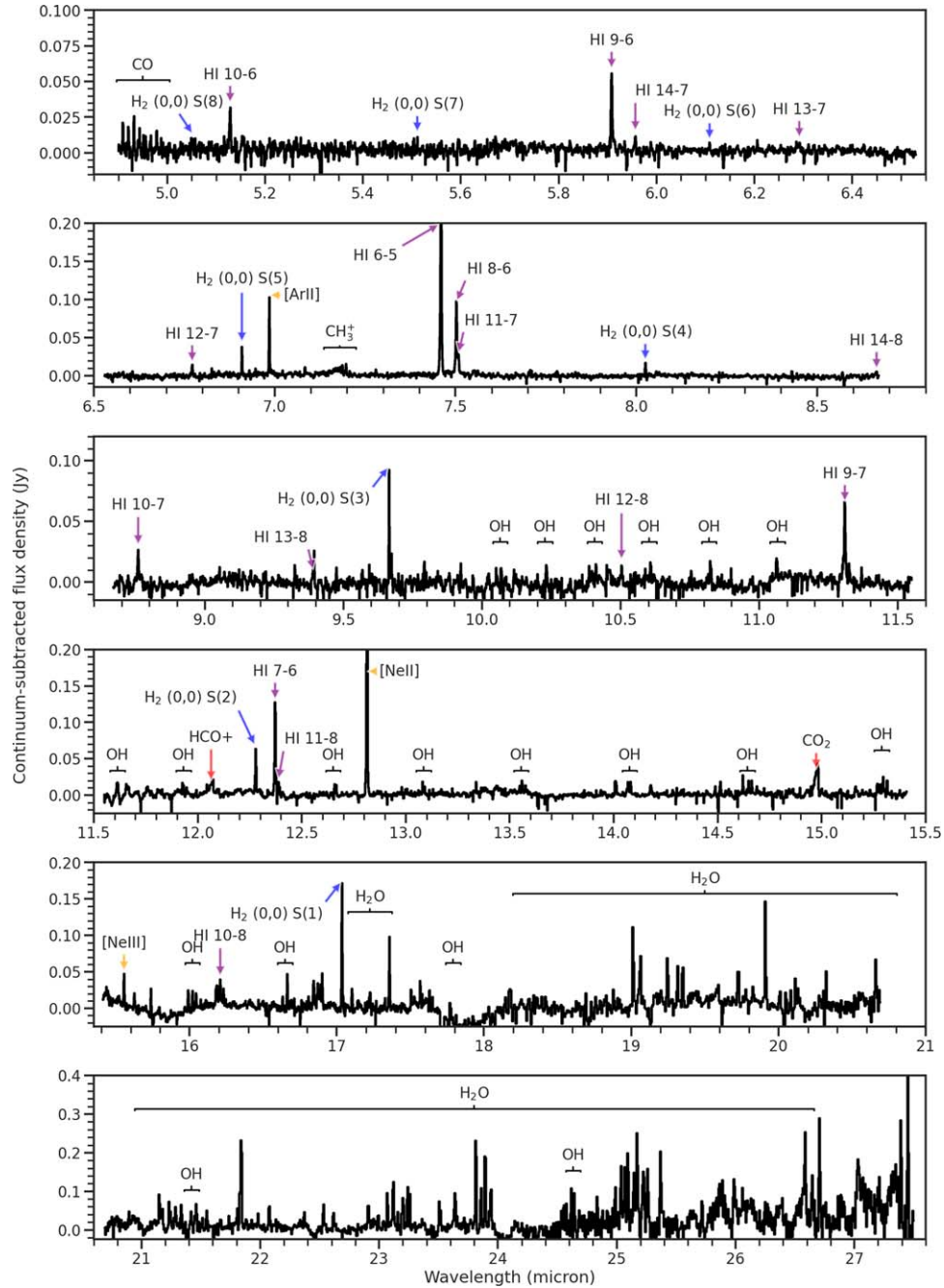


Figure 5. Continuum subtracted TW Hya MIRI spectrum with line identifications.

shorter wavelengths (see Figure 6(e)). This could indicate either (1) collisional quenching, (2) a radiative cascade of rotationally excited OH produced by water photodissociation, or (3) chemical pumping via the reaction $O+H_2$, which populates rotational levels up to $J \sim 20$ ($\lambda \gtrsim 16 \mu\text{m}$).

Molecular ions: The rovibrational band of CH_3^+ at $7.15 \mu\text{m}$ is clearly detected (Figure 6(c)); this emission band has

recently been detected for the first time by the PDRs4All team in the spectrum of a proplyd in Orion (Berné et al. 2023) and molecular data has been compiled by Changala et al. (2023). A tentative detection corresponding to the Q-branch of HCO^+ had been noted by Najita et al. (2010) and rotational line emission is clearly detected with the SMA inside $1''$ but offset to the center (inside ~ 60 au, Cleaves et al. 2015). The MIRI

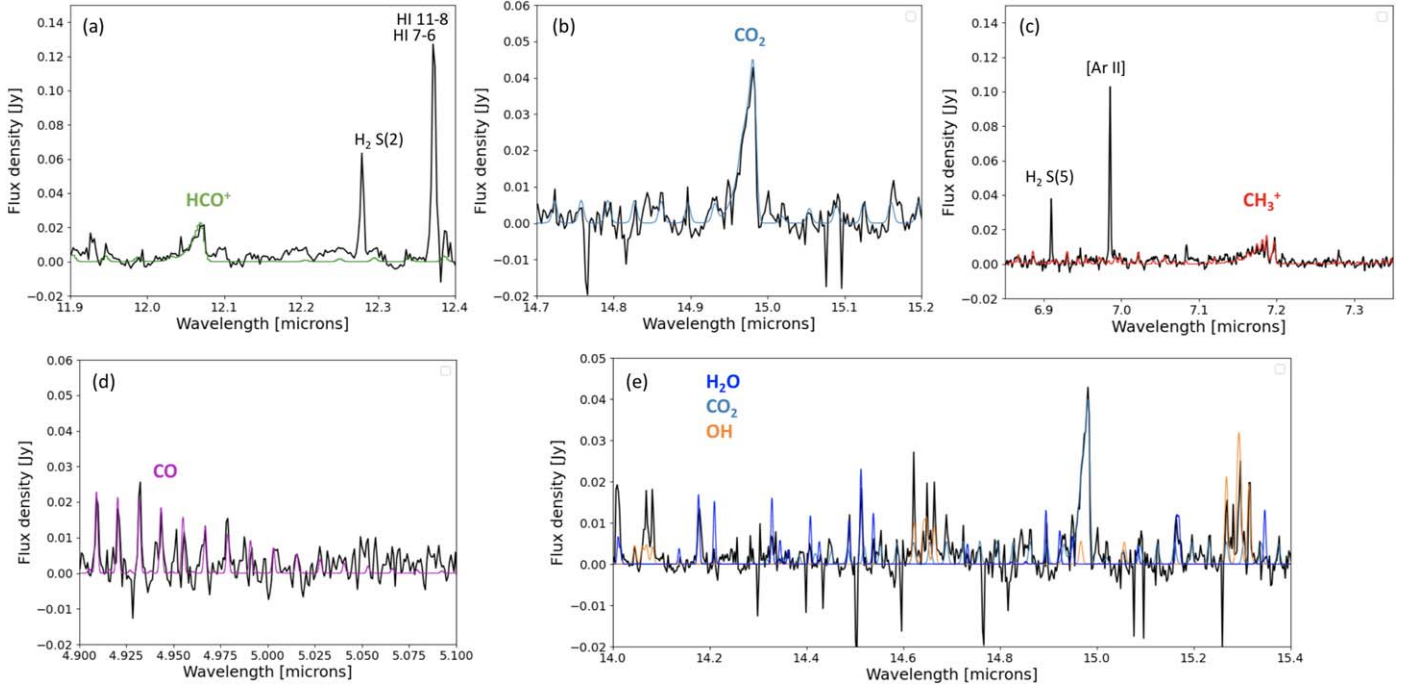


Figure 6. Continuum subtracted TW Hya MIRI spectrum (black) with (a) HCO^+ slab model (green) overplotted ($T = 250$ K, also visible the H_2 S(2) line at $12.28 \mu\text{m}$ and the H I 11-8 and 7-6 lines at 12.39 and $12.37 \mu\text{m}$), (b) CO_2 slab model (blue) overplotted ($T = 200$ K), (c) CH_3^+ slab model (red) overplotted ($T = 500$ K, also visible the H_2 S(5) line at $6.91 \mu\text{m}$ and the Ar^+ fine-structure line at $6.99 \mu\text{m}$), (d) CO slab model (magenta) overplotted ($T = 500$ K), (e) H_2O , OH and CO_2 slab models (colors indicated in legend, $T = 400, 1000, 200$ K, respectively) in the $14.0\text{--}15.4 \mu\text{m}$ wavelength range. All slab models are calculated in LTE and used only for identification of molecular emission features.

spectrum now resolves the Q-branch of HCO^+ at $12.1 \mu\text{m}$ and tentatively detects in addition several P- and R-branch lines next to it (Figure 6(a), molecular slab spectra from F. Helmich 1996, PhD thesis).

Other molecules: The high- J lines of the P-branch of the CO rovibrational band ($v = 1\text{--}0$) are well detected from P25 to P31 (Figure 6(d)); future data reduction improvements such as better fringe correction are warranted to quantitatively model the CO emission and derive upper limits for ^{13}CO . The Q-branch of CO_2 is now resolved at the MIRI spectral resolution and several P- and R-branch lines are also detected (Figure 6(b)). HCN, C_2H_2 , NH_3 , CH_3 , and CH_4 are not detected above the current noise level. Given the high S/N of our spectrum, we can now put more stringent upper limits on those molecules and we will come back to this in the next section.

6.2.2. Confronting the MIRI Spectrum with a Thermo-chemical Disk Model

So far, we have mostly used 0D slab models to guide the quantitative analysis of the MIRI spectra. These simple models are extremely powerful to build up a first level of understanding. For example, slab models show that if there were trace amounts of warm water ($N(\text{H}_2\text{O}) = 4 \times 10^{18} \text{ cm}^{-2}$,

$T = 400\text{--}600$ K) in the small inner disk of TW Hya ($\lesssim 1$ au), we would have easily detected that in our JWST/MIRI spectrum, especially at $5\text{--}8 \mu\text{m}$ (Figure 7).

In the following, we use the DIANA TW Hya disk thermo-chemical model (Woitke et al. 2019) to put a few of the key findings in the spectrum into a larger perspective. The DIANA project used the UV/optical/IR/submm photometry as well as Spitzer and Herschel/SPIRE spectra, 57 emission line fluxes, the ALMA $850 \mu\text{m}$ radial continuum emission profile and the CO $J = 3\text{--}2$ line profile to constrain the dust+gas disk structure of this object through an evolutionary fitting strategy. The DIANA disk model has been updated slightly for this work and re-run using ProDiMo. The chemical network is the large DIANA network plus D, D^+ , HD and HD^+ with 239 species and 3147 reactions compiled by Kamp et al. (2017) and updated by Kanwar et al. (2024). We changed the inner rim of the outer disk to be at 2.4 au (van Boekel et al. 2017) and adjusted the scale height to 0.06 au at 4 au and the flaring to $\beta = 1.05$ to keep the agreement with the overall observed SED. Figure 8 shows the new radial gas surface density profile, and the 2D distribution of the gas density³⁰ and temperature for the

³⁰ $n_{(\text{H})}$ is the total hydrogen number density $n(\text{H}) + 2n(\text{H}_2)$. The PDR parameter χ is the UV radiation field integrated between 912 and 2050 \AA normalized to that of Draine (1978).

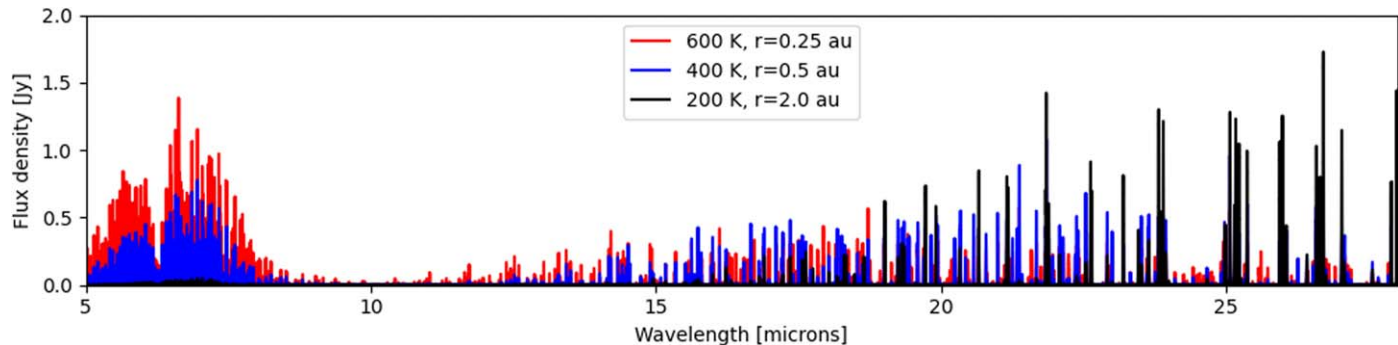


Figure 7. LTE water slab models for a column density of $4 \times 10^{18} \text{ cm}^{-2}$ (using a canonical o/p ratio of 3) and different temperatures and emitting areas πr^2 (as indicated in legend).

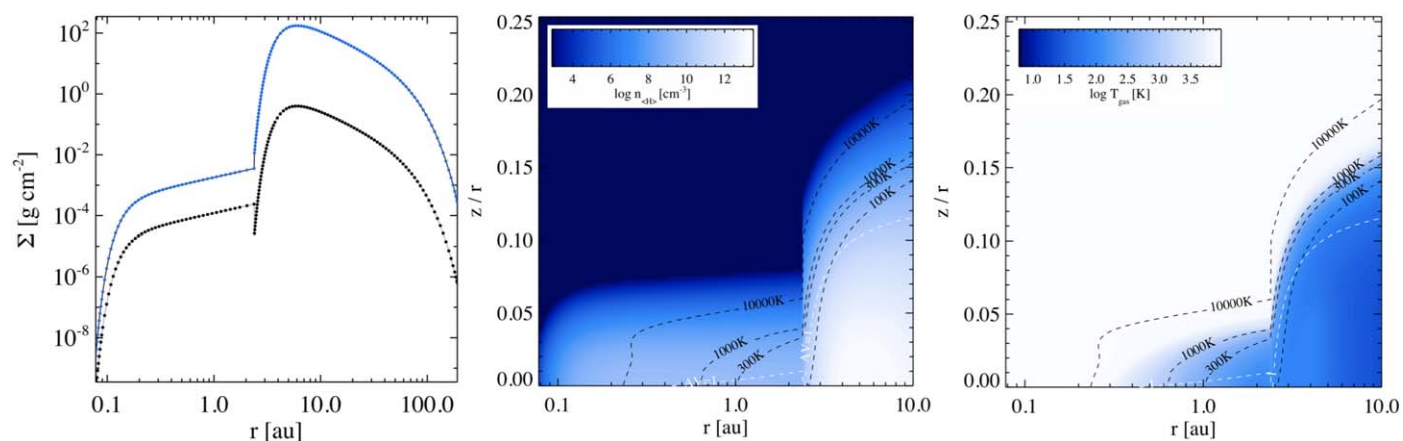


Figure 8. The radial gas (blue) and dust (black) surface density profile across the entire disk (left panel) and the density distribution (middle panel), gas temperature (right panel) inside 10 au in the adjusted TW Hya DIANA thermo-chemical disk model (elemental abundances of C, N, O depleted by a factor 50 in the inner 2.4 au). Overplotted are the gas temperature contours of 100, 300, 1000, and 10,000 K (black) and the $A_V = 1$ mag line (white).

inner 10 au. This model does not capture the radial substructure detected by SPHERE and ALMA; however, this substructure represents rather a moderate modulation of the surface density and based on previous model refinements, we do not expect this to affect much the outer disk results (e.g., Muro-Arena et al. 2018; Rab et al. 2020).

We introduced a “rounded” inner rim (gradual increase of column density toward the inner edge of the outer disk, Woitke et al. 2024) to have a radially “extended” region where the HCO^+ and CH_3^+ molecular ions are abundant (Figure 9). These molecular ions reside in the transition regime from optically thin to thick (like in PDRs) and those regions would be very geometrically thin if the column density builds up very abruptly over radius. It is interesting to note that such a “rounded” rim was also required to fit the infrared dust interferometry data (Menu et al. 2014).

The H_2 , CO ro-vib, and fine-structure lines of noble gases originate predominantly from the outer disk in our model; the H_2O lines originate predominantly from inside 2.4 au. NH_3 ,

HCN , C_2H_2 , and CO_2 emission in our model partially originate from the inner 2.4 au and partially from the inner rim of the outer disk (Figure 9). Our standard adjusted DIANA model (low ISM elemental abundances³¹) still overpredicts those features and shows some water emission at $\sim 7 \mu\text{m}$ (Figure 10, blue spectrum) undetected in our MIRI data.

Hence, we explore an elemental abundance depletion of C, N, and O by a factor 50 for the inner 2.4 au following Bosman & Banzatti (2019) and McClure et al. (2020). Reducing the elemental abundances of C and O also in the outer disk leads, in our model, to water (at longer wavelengths) and also CO emission line fluxes which are too weak compared to the observations. Such an elemental depletion in the inner disk indeed leads to much weaker CO_2 emission compared to the standard model (originating now in the inner rim of the outer disk), but the C_2H_2 is still too strong (Figure 10, orange

³¹ These abundances refer to the gas phase abundances derived for the ISM, see Table 5 of Kamp et al. (2017).

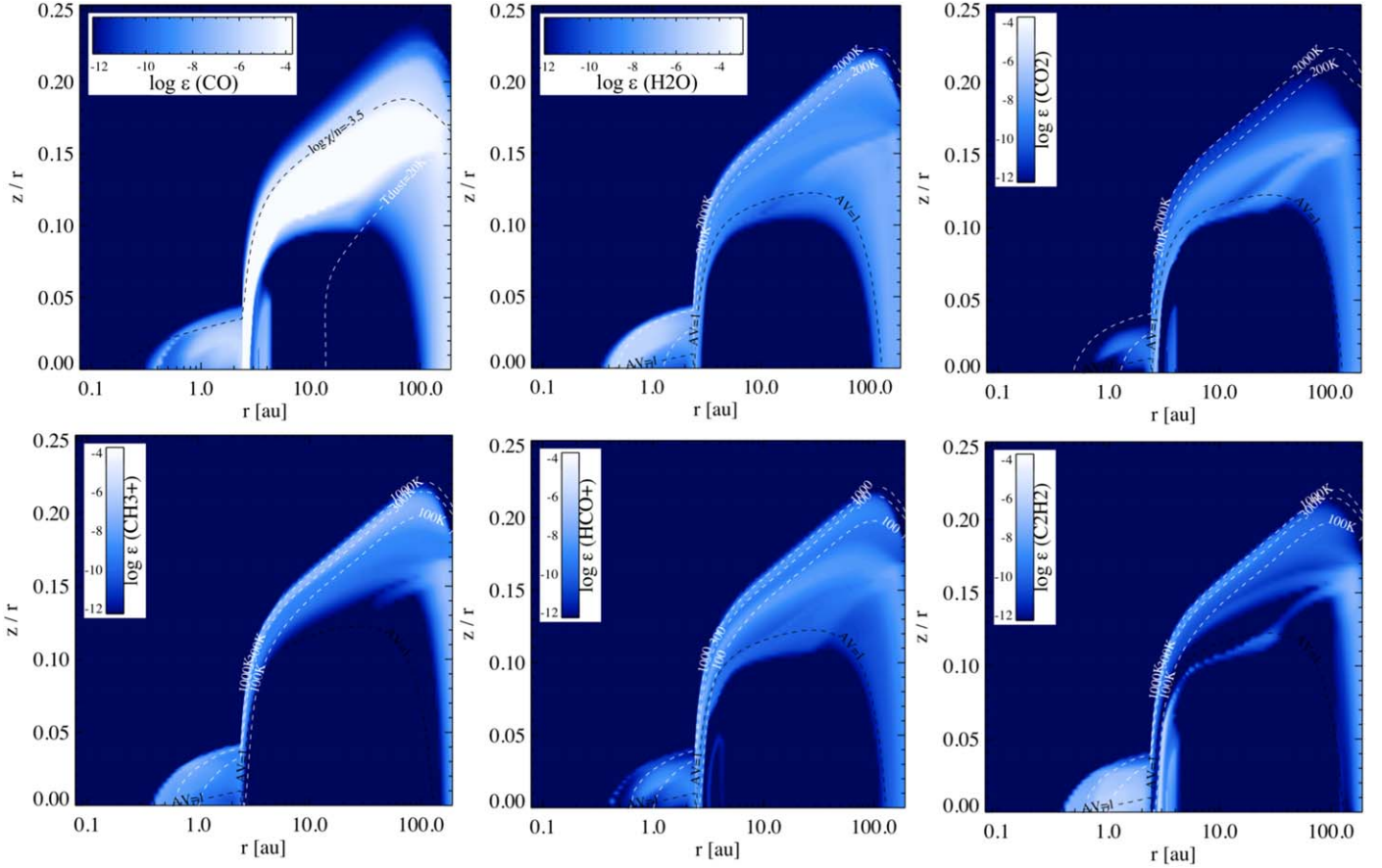


Figure 9. Selected abundance distribution of specific molecules and molecular ions in the adjusted TW Hya DIANA thermo-chemical disk model (elemental abundances of C, N, O depleted by a factor 50 in the inner 2.4 au). Overplotted are the PDR parameter $\log \chi/n_{(\text{H})}$ (see footnote in Section 6.2.2) and the dust temperature of 20 K for CO, and for all other molecules the gas temperature contours of 100, 300, and 1000 K (white) and the $A_V = 1$ mag line (black).

spectrum, and Figure 9); the bulk of the C_2H_2 emission originates inside 2.4 au despite the low C abundance.

An alternative scenario explaining the absence of water, HCN and C_2H_2 emission could be an overall lack of gas inside 2.4 au. However, if we lower the gas mass of the inner disk in the thermo-chemical model, turbulence can no longer sustain small grains in the disk surface and the $10 \mu\text{m}$ silicate feature weakens substantially (and also the continuum due to stronger settling, Figure 10, green spectrum). Our modeling approach includes the self-consistent vertical dust settling (Dubrulle et al. 1995), and so the decreasing gas density removes the pressure support for the remaining small silicate grains. If we use a gas-to-dust ratio of 0.15 instead of 15 (adjusted DIANA model), very little molecular gas remains present inside ~ 2.4 au. However, we still get weak features of C_2H_2 originating now from beyond 2.4 au; water, HCN and CO_2 emission disappears. To keep a strong silicate feature in the absence of gas, we could still adjust the grain size distribution, composition and/or scale height. In addition, the spatial distribution of small grains could

be de-coupled from the larger grains due to gap filtration effects and/or the presence of planets/planetesimals.

Given the above experiments of comparing a series of thermo-chemical disk models with varying gas-to-dust mass ratios and elemental abundances in the inner disk to the observed TW Hya MIRI spectrum, we prefer the explanation of an inner disk ($r < 2.4$ au) that contains some remnant gas with lower than ISM elemental abundances and which has a “smooth” transition from the inner to the outer disk. An exploration of a much larger parameter space including also alternative physical scenarios for the dust distribution is left for a future paper.

7. Outlook

The MINDS data presents an incredibly rich set of spectra and images which likely holds many new discoveries yet to come. One immediate example is the search for protoplanets and study of resolved disk emission in TW Hya.

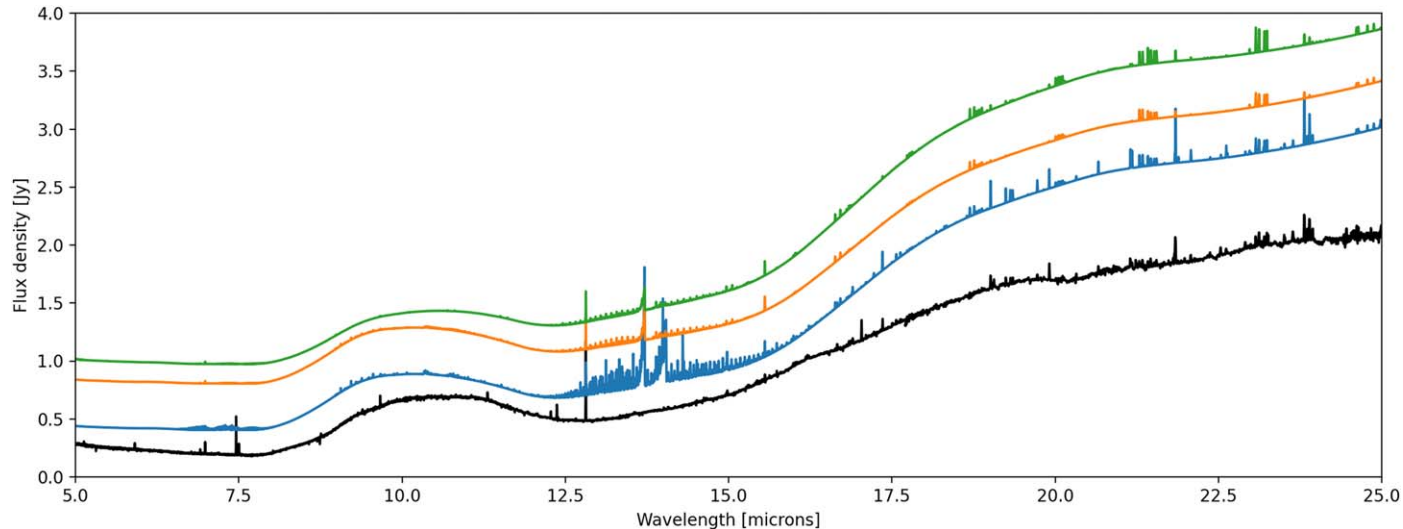


Figure 10. JWST/MIRI MRS spectrum (black) compared to the adjusted DIANA TW Hya model using a gas-to-dust mass ratio in the inner disk of 15 (blue, shifted by 0.2 Jy), and 0.15 (green, shifted by 1 Jy). The orange spectrum (shifted by 0.6 Jy) shows the model with a gas-to-dust mass ratio of 15 and the C, N and O abundances in the inner 2.4 au lowered by a factor 50.

More generally, we are now starting to search for extended line emission across the entire MINDS sample. With time, our knowledge of the instrumental PSF of MIRI/MRS will improve and we can also gather a library of observed PSFs, composed of the unresolved sources of our sample and the archive. With this in hand, the entire MIRI/MRS data could be searched for extended emission using similar strategies as the ones implemented in Ruffio et al. (2023) for NIRSpec or using PSF subtraction via a PCA approach (also common in high-contrast imaging).

Besides the individual object studies outlined in Section 6.1, we will study the broader science questions outlined in Section 1.1 on well-defined sub-samples of the MINDS sources and also use the synergy with ALMA data, interferometric data, near-IR imaging and ground-based high-spectral resolution spectra. In addition, our modeling will gradually move from simple LTE 0D slab models to more complex retrieval tools (e.g., CLiCK) and grids of forward disk models to support the interpretation of our data.

Acknowledgments

This work is based on observations made with the NASA/ESA/CSA James Webb Space Telescope. The data were obtained from the Mikulski Archive for Space Telescopes at the Space Telescope Science Institute, which is operated by the Association of Universities for Research in Astronomy, Inc., under NASA contract NAS 5-03127 for JWST. These observations are associated with the European MIRI GTO program MINDS, program #1282. I.K. acknowledges financial support and the hospitality of the Max Planck Institute for

Astronomy in Heidelberg during her visit 2023 February–June, where most of this article was compiled.

The following National and International Funding Agencies funded and supported the MIRI development: NASA; ESA; Belgian Science Policy Office (BELSPO); Centre Nationale d’Etudes Spatiales (CNES); Danish National Space Centre; Deutsches Zentrum für Luft- und Raumfahrt (DLR); Enterprise Ireland; Ministerio de Economía y Competividad; Netherlands Research School for Astronomy (NOVA); Netherlands Organisation for Scientific Research (NWO); Science and Technology Facilities Council; Swiss Space Office; Swedish National Space Agency; and UK Space Agency. A.C.G. acknowledges from PRIN-MUR 2022 20228JPA3A “The path to star and planet formation in the JWST era (PATH)” funded by NextGeneration EU and by INAF-GoG 2022 “NIR-dark Accretion Outbursts in Massive Young stellar objects (NAOMY)” and Large Grant INAF 2022 “YSOs Outflows, Disks and Accretion: toward a global framework for the evolution of planet forming systems (YODA). E.v.D. acknowledges support from the ERC grant 101019751 MOLDISK and the Danish National Research Foundation through the Center of Excellence “InterCat” (DNRF150). T.H. and K.S. acknowledge support from the European Research Council under the Horizon 2020 Framework Program via the ERC Advanced Grant Origins 83 24 28. I.K., A.M.A., and E.v.D. acknowledge support from grant TOP-1 614.001.751 from the Dutch Research Council (NWO). I.K. and J.K. acknowledge funding from H2020-MSCA-ITN-2019, grant No. 860470 (CHAMELEON). B.T. is a Laureate of the Paris Region fellowship program, which is supported by the Ile-de-France Region and has received funding under the Horizon 2020 innovation

framework program and Marie Skłodowska-Curie grant agreement No. 945298. O.A. and V.C. acknowledge funding from the Belgian F.R.S.-FNRS. I.A., D.G., O.A., V.C. and B. V. thank the Belgian Federal Science Policy Office (BELSPO) for the provision of financial support in the framework of the PRODEX Programme of the European Space Agency (ESA). L.C. acknowledges support by grant PIB2021-127718NB-I00, from the Spanish Ministry of Science and Innovation/State Agency of Research MCIN/AEI/10.13039/501100011033. T. P.R. acknowledges support from ERC grant 743029 EASY. D. R.L. acknowledges support from Science Foundation Ireland (grant No. 21/PATH-S/9339). D.B. and M.M.C. have been funded by Spanish MCIN/AEI/10.13039/501100011033 grant PID2019-107061GB-C61 and No. MDM-2017-0737. M.T. and M.V. acknowledge support from the ERC grant 101019751 MOLDISK.

ORCID iDs

Thomas Henning  <https://orcid.org/0000-0001-7455-5349>
 Inga Kamp  <https://orcid.org/0000-0002-1493-300X>
 Matthias Samland  <https://orcid.org/0000-0001-9992-4067>
 Aditya M. Arabhavi  <https://orcid.org/0000-0001-8407-4020>
 Jayatee Kanwar  <https://orcid.org/0000-0003-0386-2178>
 Ewine F. van Dishoeck  <https://orcid.org/0000-0001-7591-1907>
 Manuel Güdel  <https://orcid.org/0000-0001-9818-0588>
 Olivier Absil  <https://orcid.org/0000-0002-4006-6237>
 David Barrado  <https://orcid.org/0000-0002-5971-9242>
 Jeroen Bouwman  <https://orcid.org/0000-0003-4757-2500>
 Alessio Caratti o Garatti  <https://orcid.org/0000-0001-8876-6614>
 Vincent Geers  <https://orcid.org/0000-0003-2692-8926>
 Adrian M. Glauser  <https://orcid.org/0000-0001-9250-1547>
 Michael Mueller  <https://orcid.org/0000-0003-3217-5385>
 Göran Olofsson  <https://orcid.org/0000-0003-3747-7120>
 Tom P. Ray  <https://orcid.org/0000-0002-2110-1068>
 Silvia Scheithauer  <https://orcid.org/0000-0003-4559-0721>
 Bart Vandenbussche  <https://orcid.org/0000-0002-1368-3109>
 L. B. F. M. Waters  <https://orcid.org/0000-0002-5462-9387>
 Ioannis Argyriou  <https://orcid.org/0000-0003-2820-1077>
 Valentin Christiaens  <https://orcid.org/0000-0002-0101-8814>
 Danny Gasman  <https://orcid.org/0000-0002-1257-7742>
 Sierra L. Grant  <https://orcid.org/0000-0002-4022-4899>
 Maria Morales-Calderón  <https://orcid.org/0000-0001-9526-9499>
 Nicole Pawellek  <https://orcid.org/0000-0002-9385-9820>
 Giulia Perotti  <https://orcid.org/0000-0002-8545-6175>
 Donna Rodgers-Lee  <https://orcid.org/0000-0002-0100-1297>
 Kamber Schwarz  <https://orcid.org/0000-0002-6429-9457>

Milou Temmink  <https://orcid.org/0000-0002-7935-7445>
 Marissa Vlasblom  <https://orcid.org/0000-0002-3135-2477>

References

- ALMA Partnership, Brogan, C. L., Pérez, L. M., et al. 2015, *ApJL*, **808**, L3
 Anderson, D. E., Blake, G. A., Cleeves, L. I., et al. 2021, *ApJ*, **909**, 55
 Andrews, S. M. 2020, *ARA&A*, **58**, 483
 Andrews, S. M., Huang, J., Pérez, L. M., et al. 2018, *ApJL*, **869**, L41
 Andrews, S. M., Wilner, D. J., Zhu, Z., et al. 2016, *ApJL*, **820**, L40
 Antonellini, S., Kamp, I., Riviere-Marichalar, P., et al. 2015, *A&A*, **582**, A105
 Aoyama, Y., Ikoma, M., & Tanigawa, T. 2018, *ApJ*, **866**, 84
 Argyriou, I., Glasse, A., Law, D. R., et al. 2023, *A&A*, **675**, A111
 Argyriou, I., Wells, M., Glasse, A., et al. 2020, *A&A*, **641**, A150
 Bae, J., Isella, A., Zhu, Z., et al. 2023, in ASP Conf. Ser. 534, *Protostars and Planets VII*, ed. S. Inutsuka et al. (San Francisco: ASP), 423
 Baldovin-Saavedra, C., Audard, M., Carmona, A., et al. 2012, *A&A*, **543**, A30
 Barrado Y Navascués, D. 2006, *A&A*, **459**, 511
 Benisty, M., Bae, J., Facchini, S., et al. 2021, *ApJL*, **916**, L2
 Benisty, M., Dominik, C., Follette, K., et al. 2023, in ASP Conf. Ser. 534, *Protostars and Planets VII*, ed. S. Inutsuka et al. (San Francisco: ASP), 605
 Benisty, M., Juhasz, A., Boccaletti, A., et al. 2015, *A&A*, **578**, L6
 Bergin, E. A., Cleeves, L. I., Gorti, U., et al. 2013, *Natur*, **493**, 644
 Berné, O., Martin-Drumel, M.-A., Schroetter, I., et al. 2023, *Natur*, **621**, 56
 Bethell, T., & Bergin, E. 2009, *Sci*, **326**, 1675
 Birnstiel, T. 2023, arXiv:2312.13287
 Boccaletti, A., Cossou, C., Baudoz, P., et al. 2022, *A&A*, **667**, A165
 Bosman, A. D., & Banzatti, A. 2019, *A&A*, **632**, L10
 Bosman, A. D., Bergin, E. A., Calahan, J., & Duval, S. E. 2022a, *ApJL*, **930**, L26
 Bosman, A. D., Bergin, E. A., Calahan, J. K., & Duval, S. E. 2022b, *ApJL*, **933**, L40
 Bosman, A. D., Bruderer, S., & van Dishoeck, E. F. 2017, *A&A*, **601**, A36
 Bosman, A. D., Tielens, A. G. G. M., & van Dishoeck, E. F. 2018, *A&A*, **611**, A80
 Brown, J. M., Pontoppidan, K. M., van Dishoeck, E. F., et al. 2013, *ApJ*, **770**, 94
 Bruderer, S., Harsono, D., & van Dishoeck, E. F. 2015, *A&A*, **575**, A94
 Bruderer, S., van Dishoeck, E. F., Doty, S. D., & Herczeg, G. J. 2012, *A&A*, **541**, A91
 Burriesci, L. G. 2005, *Proc. SPIE*, **5904**, 21
 Bushouse, H., Eisenhamer, J., Dencheva, N., et al. 2022, spacetelescope/jwst: JWST v1.6.2, Zenodo, doi:10.5281/zenodo.6984366
 Calvet, N., D'Alessio, P., Hartmann, L., et al. 2002, *ApJ*, **568**, 1008
 Carr, J. S., & Najita, J. R. 2008, *Sci*, **319**, 1504
 Cazzoletti, P., van Dishoeck, E. F., Pinilla, P., et al. 2018, *A&A*, **619**, A161
 Changala, P. B., Chen, N. L., Le, H. L., et al. 2023, *A&A*, **680**, A19
 Chen, X., & Szulágyi, J. 2022, *MNRAS*, **516**, 506
 Christiaens, V., Gonzalez, C., Farkas, R., et al. 2023, *JOSS*, **8**, 4774
 Christiaens, V., Samland, M., Henning, Th., et al. 2024, arXiv:2403.04855
 Cleeves, L. I., Bergin, E. A., Qi, C., Adams, F. C., & Öberg, K. I. 2015, *ApJ*, **799**, 204
 Dent, W. R. F., Wyatt, M. C., Roberge, A., et al. 2014, *Sci*, **343**, 1490
 Draine, B. T. 1978, *ApJS*, **36**, 595
 Dubrulle, B., Morfill, G., & Sterzik, M. 1995, *Icar*, **114**, 237
 Dullemond, C. P., Juhasz, A., Pohl, A., et al. 2012 RADMC-3D: A Multi-purpose Radiative Transfer Tool, Astrophysics Source Code Library, ascl:1202.015
 Franceschi, R., Birnstiel, T., Henning, T., et al. 2022, *A&A*, **657**, A74
 Franceschi, R., Henning, T., Tabone, B., et al. 2024, arXiv:2404.11942
 Gaia Collaboration, Smart, R. L., Sarro, L. M., et al. 2021, *A&A*, **649**, A6
 Garufi, A., Podio, L., Kamp, I., et al. 2014, *A&A*, **567**, A141
 Garufi, A., Quanz, S. P., Avenhaus, H., et al. 2013, *A&A*, **560**, A105
 Gasman, D., van Dishoeck, E. F., Grant, S. L., et al. 2023, *A&A*, **679**, A117
 Gomez Gonzalez, C. A., Wertz, O., Absil, O., et al. 2017, *AJ*, **154**, 7
 Gordon, I. E., Rothman, L. S., Hargreaves, R. J., et al. 2022, *JQSRT*, **277**, 107949
 Gorti, U., & Hollenbach, D. 2004, *ApJ*, **613**, 424
 Grant, S. L., van Dishoeck, E. F., Tabone, B., et al. 2023, *ApJL*, **947**, L6

- Gratton, R., Ligi, R., Sissa, E., et al. 2019, *A&A*, **623**, A140
- Gravity Collaboration, Garcia Lopez, R., Natta, A., et al. 2020, *Natur*, **584**, 547
- GRAVITY Collaboration, Perraut, K., Labadie, L., et al. 2021, *A&A*, **655**, A73
- Gravity Collaboration, Wojtczak, J. A., Labadie, L., et al. 2023, *A&A*, **669**, A59
- Greenwood, A. J., Kamp, I., Waters, L. B. F. M., Woitke, P., & Thi, W. F. 2019, *A&A*, **626**, A6
- Hammond, I., Christiaens, V., Price, D. J., et al. 2023, *MNRAS*, **522**, L51
- Hoff, W., Henning, T., & Pfau, W. 1998, *A&A*, **336**, 242
- Jakobsen, P., Ferruit, P., Alves de Oliveira, C., et al. 2022, *A&A*, **661**, A80
- James, M. M., Pascucci, I., Liu, Y., et al. 2022, *ApJ*, **941**, 187
- Juhász, A., Henning, T., Bouwman, J., et al. 2009, *ApJ*, **695**, 1024
- Kamp, I., Henning, T., Arabhavi, A. M., et al. 2023, *FaDi*, **245**, 112
- Kamp, I., Thi, W.-F., Woitke, P., et al. 2017, *A&A*, **607**, A41
- Kamp, I., Tilling, I., Woitke, P., Thi, W., & Hogerheijde, M. 2010, *A&A*, **510**, A18
- Kanwar, J., Kamp, I., Woitke, P., et al. 2024, *A&A*, **681**, A22
- Kaeufer, T., Woitke, P., Min, M., Kamp, I., & Pinte, C. 2023, *A&A*, **672**, A30
- Kepler, M., Benisty, M., Müller, A., et al. 2018, *A&A*, **617**, A44
- Koike, C., & Shibai, H. 1990, *MNRAS*, **246**, 332
- Koike, C., Tsuchiyama, A., Shibai, H., et al. 2000, *A&A*, **363**, 1115
- Kóspál, Á., Ábrahám, P., Diehl, L., et al. 2023, *ApJL*, **945**, L7
- Labiano, A., Argyriou, I., Álvarez-Márquez, J., et al. 2021, *A&A*, **656**, A57
- Lahuis, F., van Dishoeck, E. F., Blake, G. A., et al. 2007, *ApJ*, **665**, 492
- Lisse, C. M., Chen, C. H., Wyatt, M. C., et al. 2009, *ApJ*, **701**, 2019
- Liu, Y., Pascucci, I., & Henning, T. 2019, *A&A*, **623**, A106
- Luhman, K. L. 2023, *AJ*, **165**, 269
- Mah, J., Bitsch, B., Pascucci, I., & Henning, T. 2023, *A&A*, **677**, L7
- Manara, C. F., Ansdell, M., Rosotti, G. P., et al. 2023, in *ASP Conf. Ser.* 534, *Protostars and Planets VII*, ed. S. Inutsuka et al. (San Francisco, CA: ASP), 539
- Mandell, A. M., Bast, J., van Dishoeck, E. F., et al. 2012, *ApJ*, **747**, 92
- Matthews, B. C., Krivov, A. V., Wyatt, M. C., Bryden, G., & Eiroa, C. 2014, in *Protostars and Planets VI*, ed. H. Beuther et al. (Tucson: Univ. Arizona Press), 521
- McClure, M. K., Dominik, C., & Kama, M. 2020, *A&A*, **642**, L15
- Menu, J., van Boekel, R., Henning, T., et al. 2014, *A&A*, **564**, A93
- Min, M., Dullemond, C. P., Dominik, C., de Koter, A., & Hovenier, J. W. 2009, *A&A*, **497**, 155
- Min, M., Hovenier, J. W., & de Koter, A. 2005, *A&A*, **432**, 909
- Miotello, A., Facchini, S., van Dishoeck, E. F., et al. 2019, *A&A*, **631**, A69
- Mollière, P., Molyarova, T., Bitsch, B., et al. 2022, *ApJ*, **934**, 74
- Moór, A., Curé, M., Kóspál, Á., et al. 2017, *ApJ*, **849**, 123
- Müller, A., Kepler, M., Henning, T., et al. 2018, *A&A*, **617**, L2
- Muro-Arena, G. A., Dominik, C., Waters, L. B. F. M., et al. 2018, *A&A*, **614**, A24
- Najita, J., Carr, J. S., & Mathieu, R. D. 2003, *ApJ*, **589**, 931
- Najita, J. R., Carr, J. S., Strom, S. E., et al. 2010, *ApJ*, **712**, 274
- Nomura, H., Aikawa, Y., Tsujimoto, M., Nakagawa, Y., & Millar, T. J. 2007, *ApJ*, **661**, 334
- Oberg, N., Kamp, I., Cazaux, S., Rab, C., & Czoske, O. 2023, *A&A*, **670**, A74
- Pascucci, I., Apai, D., Luhman, K., et al. 2009, *ApJ*, **696**, 143
- Pascucci, I., Herczeg, G., Carr, J. S., & Bruderer, S. 2013, *ApJ*, **779**, 178
- Pascucci, I., Hollenbach, D., Najita, J., et al. 2007, *ApJ*, **663**, 383
- Pawellek, N., & Krivov, A. V. 2015, *MNRAS*, **454**, 3207
- Pawellek, N., Moór, A., Kirchschrager, F., et al. 2024, *MNRAS*, **527**, 3559
- Perotti, G., Christiaens, V., Henning, T., et al. 2023, *Natur*, **620**, 516
- Pinte, C., Price, D. J., Ménard, F., et al. 2018, *ApJL*, **860**, L13
- Pinte, C., Teague, R., Flaherty, K., et al. 2023, in *ASP Conf. Ser.* 534, *Protostars and Planets VII*, ed. S. Inutsuka et al. (San Francisco, CA: ASP), 645
- Pontoppidan, K. M., Meijerink, R., Dullemond, C. P., & Blake, G. A. 2009, *ApJ*, **704**, 1482
- Pontoppidan, K. M., Salyk, C., Banzatti, A., et al. 2024, *ApJ*, **963**, 158
- Pontoppidan, K. M., Salyk, C., Blake, G. A., et al. 2010, *ApJ*, **720**, 887
- Posch, T., Mutschke, H., Trieloff, M., & Henning, T. 2007, *ApJ*, **656**, 615
- Qi, C., Ho, P. T. P., Wilner, D. J., et al. 2004, *ApJL*, **616**, L11
- Quanz, S. P., Amara, A., Meyer, M. R., et al. 2013, *ApJL*, **766**, L1
- Rab, C., Kamp, I., Dominik, C., et al. 2020, *A&A*, **642**, A165
- Ramírez-Tannus, M. C., Bik, A., Cuijpers, L., et al. 2023, *ApJL*, **958**, L30
- Rich, E. A., Monnier, J. D., Aarnio, A., et al. 2022, *AJ*, **164**, 109
- Rieke, M., Kelly, D., Horner, S., & NIRCeam Team 2005, *AAS Meeting Abstracts* 207, 115.09
- Rigliaco, E., Pascucci, I., Duchene, G., et al. 2015, *ApJ*, **801**, 31
- Riols, A., & Lesur, G. 2018, *A&A*, **617**, A117
- Riviere-Marichalar, P., Barrado, D., Augereau, J. C., et al. 2012, *A&A*, **546**, L8
- Roberge, A., Kamp, I., Montesinos, B., et al. 2013, *ApJ*, **771**, 69
- Ruffio, J.-B., Perrin, M. D., Hoch, K. K. W., et al. 2023, arXiv:2310.09902
- Sacco, G. G., Flaccomio, E., Pascucci, I., et al. 2012, *ApJ*, **747**, 142
- Salyk, C., Blake, G. A., Boogert, A. C. A., & Brown, J. M. 2009, *ApJ*, **699**, 330
- Salyk, C., Pontoppidan, K. M., Blake, G. A., Najita, J. R., & Carr, J. S. 2011, *ApJ*, **731**, 130
- Salyk, C., Pontoppidan, K. M., Blake, G. A., et al. 2008, *ApJL*, **676**, L49
- Schräpler, R., & Henning, T. 2004, *ApJ*, **614**, 960
- Schwarz, K. R., Henning, T., Christiaens, V., et al. 2024, *ApJ*, **962**, 15
- Song, L., Balakrishnan, N., Walker, K. M., et al. 2015, *ApJ*, **813**, 96
- Suto, H., Sogawa, H., Tachibana, S., et al. 2006, *MNRAS*, **370**, 1599
- Suttle, M. D., King, A. J., Schofield, P. F., Bates, H., & Russell, S. S. 2021, *GeCoA*, **299**, 219
- Tabone, B., Bettoni, G., van Dishoeck, E. F., et al. 2023, *NatAs*, **7**, 805
- Tabone, B., van Hemert, M. C., van Dishoeck, E. F., & Black, J. H. 2021, *A&A*, **650**, A192
- Tamura, M. 2009, in *AIP Conf. Ser.* 1158, *Exoplanets and Disks: Their Formation and Diversity*, ed. T. Usuda, M. Tamura, & M. Ishii (Melville, NY: AIP), 11
- Teague, R., Bae, J., Bergin, E. A., Birnstiel, T., & Foreman-Mackey, D. 2018, *ApJL*, **860**, L12
- Testi, L., Natta, A., Manara, C. F., et al. 2022, *A&A*, **663**, A98
- Thi, W. F., Kamp, I., Woitke, P., et al. 2013, *A&A*, **551**, A49
- Thi, W.-F., Ménard, F., Meeus, G., et al. 2011, *A&A*, **530**, L2
- Tsukagoshi, T., Nomura, H., Muto, T., et al. 2016, *ApJL*, **829**, L35
- van Boekel, R., Güdel, M., Henning, T., Lahuis, F., & Pantin, E. 2009, *A&A*, **497**, 137
- van Boekel, R., Henning, T., Menu, J., et al. 2017, *ApJ*, **837**, 132
- van der Marel, N., Cazzoletti, P., Pinilla, P., & Garufi, A. 2016, *ApJ*, **832**, 178
- van der Marel, N., van Dishoeck, E. F., Bruderer, S., et al. 2013, *Sci*, **340**, 1199
- van der Plas, G., van den Ancker, M. E., Waters, L. B. F. M., & Dominik, C. 2015, *A&A*, **574**, A75
- van der Tak, F. F. S., Black, J. H., Schöier, F. L., Jansen, D. J., & van Dishoeck, E. F. 2007, *A&A*, **468**, 627
- Vlasblom, M., van Dishoeck, E. F., Tabone, B., & Bruderer, S. 2024, *A&A*, **682**, A91
- Wells, M., Pel, J. W., Glasse, A., et al. 2015, *PASP*, **127**, 646
- Woitke, P., Kamp, I., Antonellini, S., et al. 2019, *PASP*, **131**, 064301
- Woitke, P., Kamp, I., & Thi, W.-F. 2009, *A&A*, **501**, 383
- Woitke, P., Min, M., Pinte, C., et al. 2016, *A&A*, **586**, A103
- Woitke, P., Min, M., Thi, W.-F., et al. 2018, *A&A*, **618**, A57
- Woitke, P., Thi, W. F., Arabhavi, A. M., et al. 2024, *A&A*, **683**, A219
- Wright, G. S., Rieke, G. H., Glasse, A., et al. 2023, *PASP*, **135**, 048003
- Wright, G. S., Wright, D., Goodson, G. B., et al. 2015, *PASP*, **127**, 595
- Wyatt, M. C. 2008, *ARA&A*, **46**, 339
- Zannese, M., Tabone, B., Habart, E., et al. 2023, *A&A*, **671**, A41
- Zeidler, S., Mutschke, H., & Posch, T. 2015, *ApJ*, **798**, 125
- Zhang, K., Pontoppidan, K. M., Salyk, C., & Blake, G. A. 2013, *ApJ*, **766**, 82